Chapter 9

Motion estimation

R. Szeliski, *Computer Vision*, Texts in Computer Science,
https://doi.org/10.1007/978-3-030-34372-9_9

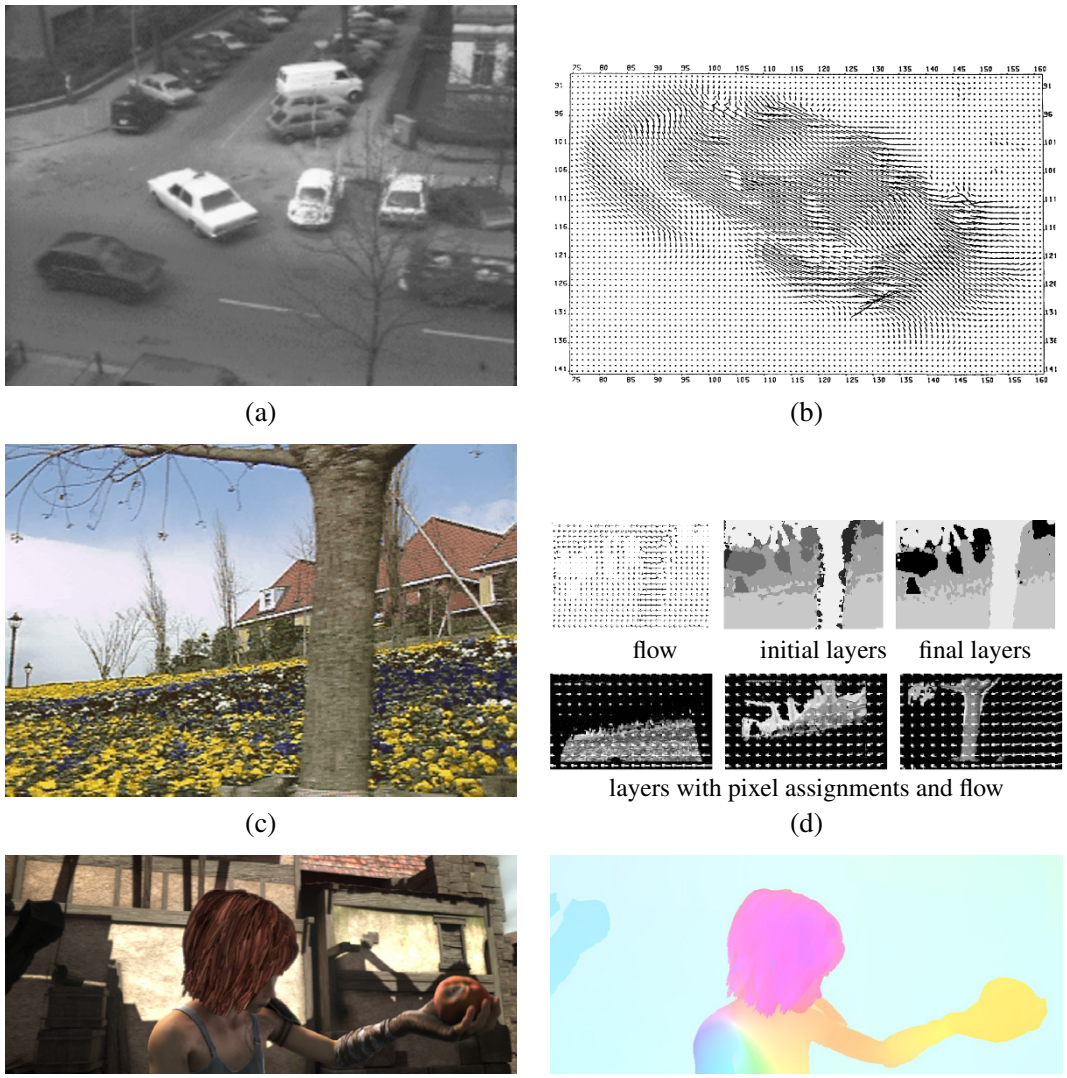

Figure 9.1 Motion estimation: (a–b) regularization-based optical flow (Nagel and Enkelmann 1986) © 1986 IEEE; (c–d) layered motion estimation (Wang and Adelson 1994) © 1994 IEEE; (e–f) sample image and ground truth flow from evaluation database (Butler, Wulff *et al.* 2012) © 2012 Springer.

Algorithms for aligning images and estimating motion in video sequences are among the most widely used in computer vision. For example, frame-rate image alignment is widely used in digital cameras to implement their image stabilization (IS) feature.

An early example of a widely used image registration algorithm is the patch-based translational alignment (optical flow) technique developed by Lucas and Kanade (1981). Variants of this algorithm are used in almost all motion-compensated video compression schemes such as MPEG/H.263 (Le Gall 1991) and HEVC/H.265 (Sullivan, Ohm *et al.* 2012). Similar parametric motion estimation algorithms have found a wide variety of applications, including video summarization (Teodosio and Bender 1993; Irani and Anandan 1998), video stabilization (Hansen, Anandan *et al.* 1994; Srinivasan, Chellappa *et al.* 2005; Matsushita, Ofek *et al.* 2006), and video compression (Irani, Hsu, and Anandan 1995; Lee, Chen *et al.* 1997). More sophisticated image registration algorithms have also been developed for medical imaging and remote sensing. Image registration techniques are surveyed by Brown (1992), Zitov'aa and Flusser (2003), Goshtasby (2005), and Szeliski (2006a).

To estimate the motion between two or more images, a suitable *error metric* must first be chosen to compare the images (Section 9.1). Once this has been established, a suitable *search* technique must be devised. The simplest technique is to exhaustively try all possible alignments, i.e., to do a *full search*. In practice, this may be too slow, so *hierarchical* coarse-to-fine techniques (Section 9.1.1) based on image pyramids are normally used. Alternatively, Fourier transforms (Section 9.1.2) can be used to speed up the computation.

To get sub-pixel precision in the alignment, *incremental* methods (Section 9.1.3) based on a Taylor series expansion of the image function are often used. These can also be applied to *parametric motion models* (Section 9.2), which model global image transformations such as rotation or shearing. Motion estimation can be made more reliable by *learning* the typical dynamics or motion statistics of the scenes or objects being tracked, e.g., the natural gait of walking people (Section 9.2). For more complex motions, piecewise parametric *spline motion models* (Section 9.2.2) can be used.

In the presence of multiple independent (and perhaps non-rigid) motions, general-purpose *optical flow* (or *optic flow*) techniques need to be used, as described in Section 9.3. In recent years, the best-performing techniques have started using deep neural networks (Section 9.3.1). For even more complex motions that include a lot of occlusions, *layered motion models* (Section 9.4), which decompose the scene into coherently moving layers, can work well. Such representations can also be used to perform video object segmentation (Section 9.4.3) and object tracking (Section 9.4.4).

In this chapter, we describe each of these techniques in more detail. Additional details can be found in review and comparative evaluation papers on motion estimation (Barron, Fleet, and Beauchemin 1994; Mitiche and Bouthemy 1996; Stiller and Konrad 1999; Szeliski 2006a; Baker, Scharstein *et al.* 2011; Sun, Yang *et al.* 2018; Janai, Güney *et al.* 2020; Hur and Roth 2020).

9.1 Translational alignment

The simplest way to establish an alignment between two images or image patches is to shift one image relative to the other. Given a *template* image $I_0(\mathbf{x})$ sampled at discrete pixel locations $\{\mathbf{x}_i = (x_i, y_i)\}$, we wish to find where it is located in image $I_1(\mathbf{x})$. A least squares solution to this problem is to find the minimum of the *sum of squared differences* (SSD) function

$$E_{\mathrm{SSD}}(\mathbf{u}) = \sum_i [I_1(\mathbf{x}_i + \mathbf{u}) - I_0(\mathbf{x}_i)]^2 = \sum_i e_i^2, \tag{9.1}$$

where $\mathbf{u} = (u, v)$ is the *displacement* and $e_i = I_1(\mathbf{x}_i + \mathbf{u}) - I_0(\mathbf{x}_i)$ is called the *residual error* (or the *displaced frame difference* in the video coding literature).[1] (We ignore for the moment the possibility that parts of I_0 may lie outside the boundaries of I_1 or be otherwise not visible.) The assumption that corresponding pixel values remain the same in the two images is often called the *brightness constancy constraint*.[2]

In general, the displacement $\mathbf{u}$ can be fractional, so a suitable interpolation function must be applied to image $I_1(\mathbf{x})$. In practice, a bilinear interpolant is often used, but bicubic interpolation can yield slightly better results (Szeliski and Scharstein 2004). Color images can be processed by summing differences across all three color channels, although it is also possible to first transform the images into a different color space or to only use the luminance (which is often done in video encoders).

Robust error metrics. We can make the above error metric more robust to outliers by replacing the squared error terms with a robust function $\rho(e_i)$ (Huber 1981; Hampel, Ronchetti *et al.* 1986; Black and Anandan 1996; Stewart 1999) to obtain

$$E_{\mathrm{SRD}}(\mathbf{u}) = \sum_i \rho(I_1(\mathbf{x}_i + \mathbf{u}) - I_0(\mathbf{x}_i)) = \sum_i \rho(e_i). \tag{9.2}$$

The robust norm $\rho(e)$ is a function that grows less quickly than the quadratic penalty associated with least squares. One such function, sometimes used in motion estimation for video coding because of its speed, is the *sum of absolute differences* (SAD) metric[3] or L_1 norm, i.e.,

$$E_{\mathrm{SAD}}(\mathbf{u}) = \sum_i |I_1(\mathbf{x}_i + \mathbf{u}) - I_0(\mathbf{x}_i)| = \sum_i |e_i|. \tag{9.3}$$

However, because this function is not differentiable at the origin, it is not well suited to gradient-descent approaches such as the ones presented in Section 9.1.3.

Instead, a smoothly varying function that is quadratic for small values but grows more slowly away from the origin is often used. Black and Rangarajan (1996) discuss a variety of such functions, including the *Geman–McClure* function,

$$\rho_{\mathrm{GM}}(x) = \frac{x^2}{1 + x^2/a^2}, \tag{9.4}$$

where a is a constant that can be thought of as an *outlier threshold*. An appropriate value for the threshold can itself be derived using robust statistics (Huber 1981; Hampel, Ronchetti *et al.* 1986; Rousseeuw and Leroy 1987), e.g., by computing the *median absolute deviation*, $MAD = \mathrm{med}_i|e_i|$, and multiplying it by 1.4 to obtain a robust estimate of the standard deviation of the inlier noise process (Stewart 1999). Barron (2019) proposes a generalized robust loss function that can model various outlier distributions and thresholds, as discussed in more detail in Sections 4.1.3 and Appendix B.3, and also has a Bayesian method for estimating the loss function parameters.

[1] The usual justification for using least squares is that it is the optimal estimate with respect to Gaussian noise. See the discussion below on robust error metrics as well as Appendix B.3.

[2] Brightness constancy (Horn 1974) is the tendency for objects to maintain their perceived brightness under varying illumination conditions.

[3] In video compression, e.g., the H.264 standard (https://www.itu.int/rec/T-REC-H.264), the sum of absolute transformed differences (SATD), which measures the differences in a frequency transform space, e.g., using a Hadamard transform, is often used, as it more accurately predicts quality (Richardson 2003).

Spatially varying weights. The error metrics above ignore that fact that for a given alignment, some of the pixels being compared may lie outside the original image boundaries. Furthermore, we may want to partially or completely downweight the contributions of certain pixels. For example, we may want to selectively "erase" some parts of an image from consideration when stitching a mosaic where unwanted foreground objects have been cut out. For applications such as background stabilization, we may want to downweight the middle part of the image, which often contains independently moving objects being tracked by the camera.

All of these tasks can be accomplished by associating a spatially varying per-pixel weight with each of the two images being matched. The error metric then becomes the weighted (or *windowed*) SSD function,

$$E_{\mathrm{WSSD}}(\mathbf{u}) = \sum_i w_0(\mathbf{x}_i) w_1(\mathbf{x}_i + \mathbf{u}) [I_1(\mathbf{x}_i + \mathbf{u}) - I_0(\mathbf{x}_i)]^2, \tag{9.5}$$

where the weighting functions w_0 and w_1 are zero outside the image boundaries.

If a large range of potential motions is allowed, the above metric can have a bias towards smaller overlap solutions. To counteract this bias, the windowed SSD score can be divided by the overlap area

$$A = \sum_i w_0(\mathbf{x}_i) w_1(\mathbf{x}_i + \mathbf{u}) \tag{9.6}$$

to compute a *per-pixel* (or mean) squared pixel error E_{WSSD}/A. The square root of this quantity is the *root mean square* intensity error

$$RMS = \sqrt{E_{\mathrm{WSSD}}/A} \tag{9.7}$$

often reported in comparative studies.

Bias and gain (exposure differences). Often, the two images being aligned were not taken with the same exposure. A simple model of linear (affine) intensity variation between the two images is the *bias and gain* model,

$$I_1(\mathbf{x} + \mathbf{u}) = (1 + \alpha) I_0(\mathbf{x}) + \beta, \tag{9.8}$$

where β is the *bias* and α is the *gain* (Lucas and Kanade 1981; Gennert 1988; Fuh and Maragos 1991; Baker, Gross, and Matthews 2003; Evangelidis and Psarakis 2008). The least squares formulation then becomes

$$E_{\mathrm{BG}}(\mathbf{u}) = \sum_i [I_1(\mathbf{x}_i + \mathbf{u}) - (1 + \alpha) I_0(\mathbf{x}_i) - \beta]^2 = \sum_i [\alpha I_0(\mathbf{x}_i) + \beta - e_i]^2. \tag{9.9}$$

Rather than taking a simple squared difference between corresponding patches, it becomes necessary to perform a *linear regression* (Appendix A.2), which is somewhat more costly. Note that for color images, it may be necessary to estimate a different bias and gain for each color channel to compensate for the automatic *color correction* performed by some digital cameras (Section 2.3.2). Bias and gain compensation are also used in video codecs, where they are known as *weighted prediction* (Richardson 2003).

A more general (spatially varying, non-parametric) model of intensity variation, which is computed as part of the registration process, is used in Negahdaripour (1998), Jia and Tang (2003), and Seitz and Baker (2009). This can be useful for dealing with local variations such as the *vignetting* caused by wide-angle lenses, wide apertures, or lens housings. It is also possible to pre-process the images before comparing their values, e.g., using band-pass filtered images (Anandan 1989;

Bergen, Anandan *et al.* 1992), or gradients (Scharstein 1994; Papenberg, Bruhn *et al.* 2006), or using other local transformations such as histograms or rank transforms (Cox, Roy, and Hingorani 1995; Zabih and Woodfill 1994), or to maximize *mutual information* (Viola and Wells III 1997; Kim, Kolmogorov, and Zabih 2003). Hirschmüller and Scharstein (2009) compare a number of these approaches and report on their relative performance in scenes with exposure differences.

Correlation. An alternative to taking intensity differences is to perform *correlation*, i.e., to maximize the *product* (or *cross-correlation*) of the two aligned images,

$$E_{\mathrm{CC}}(\mathbf{u}) = \sum_i I_0(\mathbf{x}_i) I_1(\mathbf{x}_i + \mathbf{u}). \tag{9.10}$$

At first glance, this may appear to make bias and gain modeling unnecessary, since the images will prefer to line up regardless of their relative scales and offsets. However, this is actually not true. If a very bright patch exists in $I_1(\mathbf{x})$, the maximum product may actually lie in that area.

For this reason, *normalized cross-correlation* is more commonly used,

$$E_{\mathrm{NCC}}(\mathbf{u}) = \frac{\sum_i [I_0(\mathbf{x}_i) - \overline{I_0}]\,[I_1(\mathbf{x}_i + \mathbf{u}) - \overline{I_1}]}{\sqrt{\sum_i [I_0(\mathbf{x}_i) - \overline{I_0}]^2}\sqrt{\sum_i [I_1(\mathbf{x}_i + \mathbf{u}) - \overline{I_1}]^2}}, \tag{9.11}$$

where

$$\overline{I_0} = \frac{1}{N}\sum_i I_0(\mathbf{x}_i) \qquad \text{and} \tag{9.12}$$

$$\overline{I_1} = \frac{1}{N}\sum_i I_1(\mathbf{x}_i + \mathbf{u}) \tag{9.13}$$

are the *mean images* of the corresponding patches and N is the number of pixels in the patch. The normalized cross-correlation score is always guaranteed to be in the range $[-1, 1]$, which makes it easier to handle in some higher-level applications, such as deciding which patches truly match. Normalized correlation works well when matching images taken with different exposures, e.g., when creating high dynamic range images (Section 10.2). Note, however, that the NCC score is undefined if either of the two patches has zero variance (and, in fact, its performance degrades for noisy low-contrast regions).

A variant on NCC, which is related to the bias–gain regression implicit in the matching score (9.9), is the *normalized SSD* score

$$E_{\mathrm{NSSD}}(\mathbf{u}) = \frac{1}{2}\frac{\sum_i \left[[I_0(\mathbf{x}_i) - \overline{I_0}] - [I_1(\mathbf{x}_i + \mathbf{u}) - \overline{I_1}]\right]^2}{\sqrt{\sum_i [I_0(\mathbf{x}_i) - \overline{I_0}]^2 + [I_1(\mathbf{x}_i + \mathbf{u}) - \overline{I_1}]^2}} \tag{9.14}$$

proposed by Criminisi, Shotton *et al.* (2007). In their experiments, they find that it produces comparable results to NCC, but is more efficient when applied to a large number of overlapping patches using a moving average technique (Section 3.2.2).

9.1.1 Hierarchical motion estimation

Now that we have a well-defined alignment cost function to optimize, how can we find its minimum? The simplest solution is to do a *full search* over some range of shifts, using either integer or sub-pixel

steps. This is often the approach used for *block matching* in *motion compensated video compression*, where a range of possible motions (say, ± 16 pixels) is explored.[4]

To accelerate this search process, *hierarchical motion estimation* is often used: an image pyramid (Section 3.5) is constructed and a search over a smaller number of discrete pixels (corresponding to the same range of motion) is first performed at coarser levels (Quam 1984; Anandan 1989; Bergen, Anandan *et al.* 1992). The motion estimate from one level of the pyramid is then used to initialize a smaller *local* search at the next finer level. Alternatively, several seeds (good solutions) from the coarse level can be used to initialize the fine-level search. While this is not guaranteed to produce the same result as a full search, it usually works almost as well and is much faster.

More formally, let

$$I_k^{(l)}(\mathbf{x}_j) \leftarrow \tilde{I}_k^{(l-1)}(2\mathbf{x}_j) \tag{9.15}$$

be the *decimated* image at level l obtained by subsampling (*downsampling*) a smoothed version of the image at level $l-1$. See Section 3.5 for how to perform the required downsampling (pyramid construction) without introducing too much aliasing.

At the coarsest level, we search for the best displacement $\mathbf{u}^{(l)}$ that minimizes the difference between images $I_0^{(l)}$ and $I_1^{(l)}$. This is usually done using a full search over some range of displacements $\mathbf{u}^{(l)} \in 2^{-l}[-S, S]^2$, where S is the desired *search range* at the finest (original) resolution level, optionally followed by the incremental refinement step described in Section 9.1.3.

Once a suitable motion vector has been estimated, it is used to *predict* a likely displacement

$$\hat{\mathbf{u}}^{(l-1)} \leftarrow 2\mathbf{u}^{(l)} \tag{9.16}$$

for the next finer level.[5] The search over displacements is then repeated at the finer level over a much narrower range of displacements, say $\hat{\mathbf{u}}^{(l-1)} \pm 1$, again optionally combined with an incremental refinement step (Anandan 1989). Alternatively, one of the images can be *warped* (resampled) by the current motion estimate, in which case only small incremental motions need to be computed at the finer level. A nice description of the whole process, extended to parametric motion estimation (Section 9.2), is provided by Bergen, Anandan *et al.* (1992).

9.1.2 Fourier-based alignment

When the search range corresponds to a significant fraction of the larger image (as is the case in image stitching, see Section 8.2), the hierarchical approach may not work that well, as it is often not possible to coarsen the representation too much before significant features are blurred away. In this case, a Fourier-based approach may be preferable.

Fourier-based alignment relies on the fact that the Fourier transform of a shifted signal has the same magnitude as the original signal, but a linearly varying phase (Section 3.4), i.e.,

$$\mathcal{F}\{I_1(\mathbf{x}+\mathbf{u})\} = \mathcal{F}\{I_1(\mathbf{x})\}\, e^{-ju\cdot\boldsymbol{\omega}} = \mathcal{I}_1(\boldsymbol{\omega}) e^{-ju\cdot\boldsymbol{\omega}}, \tag{9.17}$$

where $\boldsymbol{\omega}$ is the vector-valued angular frequency of the Fourier transform and we use calligraphic notation $\mathcal{I}_1(\boldsymbol{\omega}) = \mathcal{F}\{I_1(\mathbf{x})\}$ to denote the Fourier transform of a signal (Section 3.4).

[4] In stereo matching (Section 12.1.2), an explicit search over all possible disparities (i.e., a *plane sweep*) is almost always performed, as the number of search hypotheses is much smaller due to the 1D nature of the potential displacements.

[5] This doubling of displacements is only necessary if displacements are defined in integer *pixel* coordinates, which is the usual case in the literature (Bergen, Anandan *et al.* 1992). If *normalized device coordinates* (Section 2.1.4) are used instead, the displacements (and search ranges) need not change from level to level, although the step sizes will need to be adjusted, to keep search steps of roughly one pixel or less.

Another useful property of Fourier transforms is that convolution in the spatial domain corresponds to multiplication in the Fourier domain (Section 3.4).[6] The Fourier transform of the cross-correlation function E_{CC} can thus be written as

$$\mathcal{F}\{E_{\mathrm{CC}}(\mathbf{u})\} = \mathcal{F}\left\{\sum_i I_0(\mathbf{x}_i) I_1(\mathbf{x}_i + \mathbf{u})\right\} = \mathcal{F}\{I_0(\mathbf{u}) \bar{*} I_1(\mathbf{u})\} = \mathcal{I}_0(\boldsymbol{\omega}) \mathcal{I}_1^*(\boldsymbol{\omega}), \tag{9.18}$$

where

$$f(\mathbf{u}) \bar{*} g(\mathbf{u}) = \sum_i f(\mathbf{x}_i) g(\mathbf{x}_i + \mathbf{u}) \tag{9.19}$$

is the *correlation* function, i.e., the convolution of one signal with the reverse of the other, and $\mathcal{I}_1^*(\boldsymbol{\omega})$ is the *complex conjugate* of $\mathcal{I}_1(\boldsymbol{\omega})$. This is because convolution is defined as the summation of one signal with the reverse of the other (Section 3.4).

To efficiently evaluate E_{CC} over the range of all possible values of $\mathbf{u}$, we take the Fourier transforms of both images $I_0(\mathbf{x})$ and $I_1(\mathbf{x})$, multiply both transforms together (after conjugating the second one), and take the inverse transform of the result. The Fast Fourier Transform algorithm can compute the transform of an $N \times M$ image in $\mathrm{O}(NM \log NM)$ operations (Bracewell 1986). This can be significantly faster than the $\mathrm{O}(N^2 M^2)$ operations required to do a full search when the full range of image overlaps is considered.

While Fourier-based convolution is often used to accelerate the computation of image correlations, it can also be used to accelerate the sum of squared differences function (and its variants). Consider the SSD formula given in (9.1). Its Fourier transform can be written as

$$\begin{aligned}\mathcal{F}\{E_{\mathrm{SSD}}(\mathbf{u})\} &= \mathcal{F}\left\{\sum_i [I_1(\mathbf{x}_i + \mathbf{u}) - I_0(\mathbf{x}_i)]^2\right\} \\ &= \delta(\boldsymbol{\omega}) \sum_i [I_0^2(\mathbf{x}_i) + I_1^2(\mathbf{x}_i)] - 2\mathcal{I}_0(\boldsymbol{\omega}) \mathcal{I}_1^*(\boldsymbol{\omega}).\end{aligned} \tag{9.20}$$

Thus, the SSD function can be computed by taking twice the correlation function and subtracting it from the sum of the energies in the two images (or patches).

Windowed correlation. Unfortunately, the Fourier convolution theorem only applies when the summation over $\mathbf{x}_i$ is performed over *all* the pixels in both images, using a circular shift of the image when accessing pixels outside the original boundaries. While this is acceptable for small shifts and comparably sized images, it makes no sense when the images overlap by a small amount or one image is a small subset of the other.

In that case, the cross-correlation function should be replaced with a *windowed* (weighted) cross-correlation function,

$$E_{\mathrm{WCC}}(\mathbf{u}) = \sum_i w_0(\mathbf{x}_i) I_0(\mathbf{x}_i)\, w_1(\mathbf{x}_i + \mathbf{u}) I_1(\mathbf{x}_i + \mathbf{u}), \tag{9.21}$$

$$= [w_0(\mathbf{x}) I_0(\mathbf{x})] \bar{*} [w_1(\mathbf{x}) I_1(\mathbf{x})] \tag{9.22}$$

where the weighting functions w_0 and w_1 are zero outside the valid ranges of the images and both images are padded so that circular shifts return 0 values outside the original image boundaries.

[6] In fact, the Fourier shift property (9.17) derives from the convolution theorem by observing that shifting is equivalent to convolution with a displaced delta function $\delta(\mathbf{x} - \mathbf{u})$.

An even more interesting case is the computation of the *weighted* SSD function introduced in Equation (9.5),

$$E_{\mathrm{WSSD}}(\mathbf{u}) = \sum_i w_0(\mathbf{x}_i) w_1(\mathbf{x}_i + \mathbf{u}) [I_1(\mathbf{x}_i + \mathbf{u}) - I_0(\mathbf{x}_i)]^2. \tag{9.23}$$

Expanding this as a sum of correlations and deriving the appropriate set of Fourier transforms is left for Exercise 9.1.

The same kind of derivation can also be applied to the bias–gain corrected sum of squared difference function E_{BG} (9.9). Again, Fourier transforms can be used to efficiently compute all the correlations needed to perform the linear regression in the bias and gain parameters in order to estimate the exposure-compensated difference for each potential shift (Exercise 9.1). It is also possible to use Fourier transforms to estimate the rotation and scale between two patches that are centered on the same pixel, as described in De Castro and Morandi (1987) and Szeliski (2010, Section 8.1.2).

Phase correlation. A variant of regular correlation (9.18) that is sometimes used for motion estimation is *phase correlation* (Kuglin and Hines 1975; Brown 1992). Here, the spectrum of the two signals being matched is *whitened* by dividing each per-frequency product in (9.18) by the magnitudes of the Fourier transforms,

$$\mathcal{F}\{E_{\mathrm{PC}}(\mathbf{u})\} = \frac{\mathcal{I}_0(\boldsymbol{\omega}) \mathcal{I}_1^*(\boldsymbol{\omega})}{\|\mathcal{I}_0(\boldsymbol{\omega})\| \|\mathcal{I}_1(\boldsymbol{\omega})\|} \tag{9.24}$$

before taking the final inverse Fourier transform. In the case of noiseless signals with perfect (cyclic) shift, we have $I_1(\mathbf{x} + \mathbf{u}) = I_0(\mathbf{x})$ and hence, from Equation (9.17), we obtain

$$\begin{aligned} \mathcal{F}\{I_1(\mathbf{x} + \mathbf{u})\} &= \mathcal{I}_1(\boldsymbol{\omega}) e^{-2\pi j u \cdot \boldsymbol{\omega}} = \mathcal{I}_0(\boldsymbol{\omega}) \quad \text{and} \\ \mathcal{F}\{E_{\mathrm{PC}}(\mathbf{u})\} &= e^{-2\pi j u \cdot \boldsymbol{\omega}}. \end{aligned} \tag{9.25}$$

The output of phase correlation (under ideal conditions) is therefore a single spike (impulse) located at the correct value of $\mathbf{u}$, which (in principle) makes it easier to find the correct estimate.

Phase correlation has a reputation in some quarters of outperforming regular correlation, but this behavior depends on the characteristics of the signals and noise. If the original images are contaminated by noise in a narrow frequency band (e.g., low-frequency noise or peaked frequency "hum"), the whitening process effectively de-emphasizes the noise in these regions. However, if the original signals have very low signal-to-noise ratio at some frequencies (say, two blurry or low-textured images with lots of high-frequency noise), the whitening process can actually decrease performance (see Exercise 9.1).

Gradient cross-correlation has emerged as a promising alternative to phase correlation (Argyriou and Vlachos 2003), although further systematic studies are probably warranted. Phase correlation has also been studied by Fleet and Jepson (1990) as a method for estimating general optical flow and stereo disparity.

9.1.3 Incremental refinement

The techniques described up till now can estimate alignment to the nearest pixel (or potentially fractional pixel if smaller search steps are used). In general, image stabilization and stitching applications require much higher accuracies to obtain acceptable results.

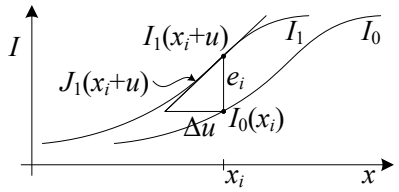

Figure 9.2 Taylor series approximation of a function and the incremental computation of the optical flow correction amount. $\mathbf{J}_1(\mathbf{x}_i + \mathbf{u})$ is the image gradient at $(\mathbf{x}_i + \mathbf{u})$ and e_i is the current intensity difference.

To obtain better *sub-pixel* estimates, we can use one of several techniques described by Tian and Huhns (1986). One possibility is to evaluate several discrete (integer or fractional) values of (u, v) around the best value found so far and to *interpolate* the matching score to find an analytic minimum (Szeliski and Scharstein 2004).

A more commonly used approach, first proposed by Lucas and Kanade (1981), is to perform *gradient descent* on the SSD energy function (9.1), using a Taylor series expansion of the image function (Figure 9.2),

$$E_{\mathrm{LK-SSD}}(\mathbf{u} + \Delta\mathbf{u}) = \sum_i [I_1(\mathbf{x}_i + \mathbf{u} + \Delta\mathbf{u}) - I_0(\mathbf{x}_i)]^2 \tag{9.26}$$

$$\approx \sum_i [I_1(\mathbf{x}_i + \mathbf{u}) + \mathbf{J}_1(\mathbf{x}_i + \mathbf{u})\Delta\mathbf{u} - I_0(\mathbf{x}_i)]^2 \tag{9.27}$$

$$= \sum_i [\mathbf{J}_1(\mathbf{x}_i + \mathbf{u})\Delta\mathbf{u} + e_i]^2, \tag{9.28}$$

where

$$\mathbf{J}_1(\mathbf{x}_i + \mathbf{u}) = \nabla I_1(\mathbf{x}_i + \mathbf{u}) = \left(\frac{\partial I_1}{\partial x}, \frac{\partial I_1}{\partial y}\right)(\mathbf{x}_i + \mathbf{u}) \tag{9.29}$$

is the *image gradient* or *Jacobian* at $(\mathbf{x}_i + \mathbf{u})$ and

$$e_i = I_1(\mathbf{x}_i + \mathbf{u}) - I_0(\mathbf{x}_i), \tag{9.30}$$

first introduced in (9.1), is the current intensity error.[7] The gradient at a particular sub-pixel location $(\mathbf{x}_i + \mathbf{u})$ can be computed using a variety of techniques, the simplest of which is simply to take the horizontal and vertical differences between pixels $\mathbf{x}$ and $\mathbf{x} + (1, 0)$ or $\mathbf{x} + (0, 1)$. More sophisticated derivatives can sometimes lead to noticeable performance improvements.

The linearized form of the incremental update to the SSD error (9.28) is often called the *optical flow constraint* or *brightness constancy constraint* equation (Horn and Schunck 1981)

$$I_x u + I_y v + I_t = 0, \tag{9.31}$$

where the subscripts in I_x and I_y denote spatial derivatives, and I_t is called the *temporal derivative*, which makes sense if we are computing instantaneous velocity in a video sequence. When squared and summed or integrated over a region, it can be used to compute optical flow (Horn and Schunck 1981).

The above least squares problem (9.28) can be minimized by solving the associated *normal equations* (Appendix A.2),

$$\mathbf{A}\Delta\mathbf{u} = \mathbf{b} \tag{9.32}$$

[7] We follow the convention, commonly used in robotics and by Baker and Matthews (2004), that derivatives with respect to (column) vectors result in row vectors, so that fewer transposes are needed in the formulas.

where

$$\mathbf{A} = \sum_i \mathbf{J}_1^T(\mathbf{x}_i + \mathbf{u})\mathbf{J}_1(\mathbf{x}_i + \mathbf{u}) \tag{9.33}$$

and

$$\mathbf{b} = -\sum_i e_i \mathbf{J}_1^T(\mathbf{x}_i + \mathbf{u}) \tag{9.34}$$

are called the (Gauss–Newton approximation of the) *Hessian* and *gradient-weighted residual vector*, respectively.[8] These matrices are also often written as

$$\mathbf{A} = \begin{bmatrix} \sum I_x^2 & \sum I_x I_y \\ \sum I_x I_y & \sum I_y^2 \end{bmatrix} \quad \text{and} \quad \mathbf{b} = -\begin{bmatrix} \sum I_x I_t \\ \sum I_y I_t \end{bmatrix}. \tag{9.35}$$

The gradients required for $\mathbf{J}_1(\mathbf{x}_i + \mathbf{u})$ can be evaluated at the same time as the image warps required to estimate $I_1(\mathbf{x}_i + \mathbf{u})$ (Section 3.6.1 (3.75)) and, in fact, are often computed as a side-product of image interpolation. If efficiency is a concern, these gradients can be replaced by the gradients in the *template* image,

$$\mathbf{J}_1(\mathbf{x}_i + \mathbf{u}) \approx \mathbf{J}_0(\mathbf{x}_i), \tag{9.36}$$

because near the correct alignment, the template and displaced target images should look similar. This has the advantage of allowing the precomputation of the Hessian and Jacobian images, which can result in significant computational savings (Hager and Belhumeur 1998; Baker and Matthews 2004). A further reduction in computation can be obtained by writing the warped image $I_1(\mathbf{x}_i + \mathbf{u})$ used to compute e_i in (9.30) as a convolution of a sub-pixel interpolation filter with the discrete samples in I_1 (Peleg and Rav-Acha 2006). Precomputing the inner product between the gradient field and shifted version of I_1 allows the iterative re-computation of e_i to be performed in constant time (independent of the number of pixels).

The effectiveness of the above incremental update rule relies on the quality of the Taylor series approximation. When far away from the true displacement (say, 1–2 pixels), several iterations may be needed. It is possible, however, to estimate a value for $\mathbf{J}_1$ using a least squares fit to a series of larger displacements to increase the range of convergence (Jurie and Dhome 2002) or to "learn" a special-purpose recognizer for a given patch (Avidan 2001; Williams, Blake, and Cipolla 2003; Lepetit, Pilet, and Fua 2006; Hinterstoisser, Benhimane *et al.* 2008; Özuysal, Calonder *et al.* 2010) as discussed in Section 7.1.5.

A commonly used stopping criterion for incremental updating is to monitor the magnitude of the displacement correction $\|\mathbf{u}\|$ and to stop when it drops below a certain threshold (say, $1/10$ of a pixel). For larger motions, it is usual to combine the incremental update rule with a hierarchical coarse-to-fine search strategy, as described in Section 9.1.1.

Conditioning and aperture problems. Sometimes, the inversion of the linear system (9.32) can be poorly conditioned because of lack of two-dimensional texture in the patch being aligned. A commonly occurring example of this is the *aperture problem*, first identified in some of the early papers on optical flow (Horn and Schunck 1981) and then studied more extensively by Anandan (1989). Consider an image patch that consists of a slanted edge moving to the right (Figure 7.4). Only the *normal* component of the velocity (displacement) can be reliably recovered in this case.

[8] The true Hessian is the full second derivative of the error function E, which may not be positive definite—see Section 8.1.3 and Appendix A.3.

This manifests itself in (9.32) as a *rank-deficient* matrix $\mathbf{A}$, i.e., one whose smaller eigenvalue is very close to zero.[9]

When Equation (9.32) is solved, the component of the displacement along the edge is very poorly conditioned and can result in wild guesses under small noise perturbations. One way to mitigate this problem is to add a *prior* (soft constraint) on the expected range of motions (Simoncelli, Adelson, and Heeger 1991; Baker, Gross, and Matthews 2004; Govindu 2006). This can be accomplished by adding a small value to the diagonal of $\mathbf{A}$, which essentially biases the solution towards smaller $\Delta\mathbf{u}$ values that still (mostly) minimize the squared error.

However, the pure Gaussian model assumed when using a simple (fixed) quadratic prior, as in Simoncelli, Adelson, and Heeger (1991), does not always hold in practice, e.g., because of aliasing along strong edges (Triggs 2004). For this reason, it may be prudent to add some small fraction (say, 5%) of the larger eigenvalue to the smaller one before doing the matrix inversion.

Uncertainty modeling. The reliability of a particular patch-based motion estimate can be captured more formally with an *uncertainty model*. The simplest such model is a *covariance matrix*, which captures the expected variance in the motion estimate in all possible directions. As discussed in Section 8.1.4 and Appendix B.6, under small amounts of additive Gaussian noise, it can be shown that the covariance matrix $\mathbf{\Sigma_u}$ is proportional to the inverse of the Hessian $\mathbf{A}$,

$$\mathbf{\Sigma_u} = \sigma_n^2 \mathbf{A}^{-1}, \tag{9.37}$$

where σ_n^2 is the variance of the additive Gaussian noise (Anandan 1989; Matthies, Kanade, and Szeliski 1989; Szeliski 1989).

For larger amounts of noise, the linearization performed by the Lucas–Kanade algorithm in (9.28) is only approximate, so the above quantity becomes a *Cramer–Rao lower bound* on the true covariance. Thus, the minimum and maximum eigenvalues of the Hessian $\mathbf{A}$ can now be interpreted as the (scaled) inverse variances in the least-certain and most-certain directions of motion. (A more detailed analysis using a more realistic model of image noise is given by Steele and Jaynes (2005).) Figure 7.5 shows the local SSD surfaces for three different pixel locations in an image. As you can see, the surface has a clear minimum in the highly textured region and suffers from the aperture problem near the strong edge.

Bias and gain, weighting, and robust error metrics. The Lucas–Kanade update rule can also be applied to the bias–gain equation (9.9) to obtain

$$E_{\mathrm{LK-BG}}(\mathbf{u}+\Delta\mathbf{u}) = \sum_i [\mathbf{J}_1(\mathbf{x}_i+\mathbf{u})\Delta\mathbf{u} + e_i - \alpha I_0(\mathbf{x}_i) - \beta]^2 \tag{9.38}$$

(Lucas and Kanade 1981; Gennert 1988; Fuh and Maragos 1991; Baker, Gross, and Matthews 2003). The resulting 4×4 system of equations can be solved to simultaneously estimate the translational displacement update $\Delta\mathbf{u}$ and the bias and gain parameters β and α.

A similar formulation can be derived for images (templates) that have a *linear appearance variation*,

$$I_1(\mathbf{x}+\mathbf{u}) \approx I_0(\mathbf{x}) + \sum_j \lambda_j B_j(\mathbf{x}), \tag{9.39}$$

[9] The matrix $\mathbf{A}$ is by construction always guaranteed to be symmetric positive semi-definite, i.e., it has real non-negative eigenvalues.

where the $B_j(\mathbf{x})$ are the *basis images* and the λ_j are the unknown coefficients (Hager and Belhumeur 1998; Baker, Gross *et al.* 2003; Baker, Gross, and Matthews 2003). Potential linear appearance variations include illumination changes (Hager and Belhumeur 1998) and small non-rigid deformations (Black and Jepson 1998; Kambhamettu, Goldgof *et al.* 2003).

A weighted (windowed) version of the Lucas–Kanade algorithm is also possible:

$$E_{\mathrm{LK-WSSD}}(\mathbf{u}+\Delta\mathbf{u}) = \sum_i w_0(\mathbf{x}_i) w_1(\mathbf{x}_i+\mathbf{u})[\mathbf{J}_1(\mathbf{x}_i+\mathbf{u})\Delta\mathbf{u} + e_i]^2. \tag{9.40}$$

Note that here, in deriving the Lucas–Kanade update from the original weighted SSD function (9.5), we have neglected taking the derivative of the $w_1(\mathbf{x}_i+\mathbf{u})$ weighting function with respect to $\mathbf{u}$, which is usually acceptable in practice, especially if the weighting function is a binary mask with relatively few transitions.

Baker, Gross *et al.* (2003) only use the $w_0(\mathbf{x})$ term, which is reasonable if the two images have the same extent and no (independent) cutouts in the overlap region. They also discuss the idea of making the weighting proportional to $\nabla I(\mathbf{x})$, which helps for very noisy images, where the gradient itself is noisy. Similar observations, formulated in terms of *total least squares* (Van Huffel and Vandewalle 1991; Van Huffel and Lemmerling 2002), have been made by other researchers studying optical flow (Weber and Malik 1995; Bab-Hadiashar and Suter 1998b; Mühlich and Mester 1998). Baker, Gross *et al.* (2003) show how evaluating Equation (9.40) at just the *most reliable* (highest gradient) pixels does not significantly reduce performance for large enough images, even if only 5–10% of the pixels are used. (This idea was originally proposed by Dellaert and Collins (1999), who used a more sophisticated selection criterion.)

The Lucas–Kanade incremental refinement step can also be applied to the robust error metric introduced in Section 9.1,

$$E_{\mathrm{LK-SRD}}(\mathbf{u}+\Delta\mathbf{u}) = \sum_i \rho(\mathbf{J}_1(\mathbf{x}_i+\mathbf{u})\Delta\mathbf{u} + e_i), \tag{9.41}$$

which can be solved using the *iteratively reweighted least squares* technique described in Section 8.1.4.

9.2 Parametric motion

Many image alignment tasks, for example image stitching with handheld cameras, require the use of more sophisticated motion models, as described in Section 2.1.1. As these models, e.g., affine deformations, typically have more parameters than pure translation, a full search over the possible range of values is impractical. Instead, the incremental Lucas–Kanade algorithm can be generalized to parametric motion models and used in conjunction with a hierarchical search algorithm (Lucas and Kanade 1981; Rehg and Witkin 1991; Fuh and Maragos 1991; Bergen, Anandan *et al.* 1992; Shashua and Toelg 1997; Shashua and Wexler 2001; Baker and Matthews 2004).

For parametric motion, instead of using a single constant translation vector $\mathbf{u}$, we use a spatially varying *motion field* or *correspondence map*, $\mathbf{x}'(\mathbf{x};\mathbf{p})$, parameterized by a low-dimensional vector $\mathbf{p}$, where $\mathbf{x}'$ can be any of the motion models presented in Section 2.1.1. The parametric incremental

motion update rule now becomes

$$E_{\mathrm{LK-PM}}(\mathbf{p}+\Delta\mathbf{p}) = \sum_i [I_1(\mathbf{x}'(\mathbf{x}_i;\mathbf{p}+\Delta\mathbf{p})) - I_0(\mathbf{x}_i)]^2 \tag{9.42}$$

$$\approx \sum_i [I_1(\mathbf{x}'_i) + \mathbf{J}_1(\mathbf{x}'_i)\Delta\mathbf{p} - I_0(\mathbf{x}_i)]^2 \tag{9.43}$$

$$= \sum_i [\mathbf{J}_1(\mathbf{x}'_i)\Delta\mathbf{p} + e_i]^2, \tag{9.44}$$

where the Jacobian is now

$$\mathbf{J}_1(\mathbf{x}'_i) = \frac{\partial I_1}{\partial \mathbf{p}} = \nabla I_1(\mathbf{x}'_i)\frac{\partial \mathbf{x}'}{\partial \mathbf{p}}(\mathbf{x}_i), \tag{9.45}$$

i.e., the product of the image gradient ∇I_1 with the Jacobian of the correspondence field, $\mathbf{J}_{x'} = \partial \mathbf{x}'/\partial \mathbf{p}$.

The motion Jacobians $\mathbf{J}_{\mathbf{x}'}$ for the 2D planar transformations introduced in Section 2.1.1 and Table 2.1 are given in Table 8.1. Note how we have re-parameterized the motion matrices so that they are always the identity at the origin $\mathbf{p} = 0$. This becomes useful later, when we talk about the compositional and inverse compositional algorithms. (It also makes it easier to impose priors on the motions.)

For parametric motion, the (Gauss–Newton) *Hessian* and *gradient-weighted residual vector* become

$$\mathbf{A} = \sum_i \mathbf{J}^T_{\mathbf{x}'}(\mathbf{x}_i)[\nabla I_1^T(\mathbf{x}'_i)\nabla I_1(\mathbf{x}'_i)]\mathbf{J}_{\mathbf{x}'}(\mathbf{x}_i) \tag{9.46}$$

and

$$\mathbf{b} = -\sum_i \mathbf{J}^T_{\mathbf{x}'}(\mathbf{x}_i)[e_i \nabla I_1^T(\mathbf{x}'_i)]. \tag{9.47}$$

Note how the expressions inside the square brackets are the same ones evaluated for the simpler translational motion case (9.33–9.34).

Patch-based approximation. The computation of the Hessian and residual vectors for parametric motion can be significantly more expensive than for the translational case. For parametric motion with n parameters and N pixels, the accumulation of $\mathbf{A}$ and $\mathbf{b}$ takes $\mathrm{O}(n^2 N)$ operations (Baker and Matthews 2004). One way to reduce this by a significant amount is to divide the image up into smaller sub-blocks (patches) P_j and to only accumulate the simpler 2×2 quantities inside the square brackets at the pixel level (Shum and Szeliski 2000),

$$\mathbf{A}_j = \sum_{i \in P_j} \nabla I_1^T(\mathbf{x}'_i)\nabla I_1(\mathbf{x}'_i) \tag{9.48}$$

$$\mathbf{b}_j = \sum_{i \in P_j} e_i \nabla I_1^T(\mathbf{x}'_i). \tag{9.49}$$

The full Hessian and residual can then be approximated as

$$\mathbf{A} \approx \sum_j \mathbf{J}^T_{\mathbf{x}'}(\hat{\mathbf{x}}_j)[\sum_{i \in P_j} \nabla I_1^T(\mathbf{x}'_i)\nabla I_1(\mathbf{x}'_i)]\mathbf{J}_{\mathbf{x}'}(\hat{\mathbf{x}}_j) = \sum_j \mathbf{J}^T_{\mathbf{x}'}(\hat{\mathbf{x}}_j)\mathbf{A}_j\mathbf{J}_{\mathbf{x}'}(\hat{\mathbf{x}}_j) \tag{9.50}$$

and

$$\mathbf{b} \approx -\sum_j \mathbf{J}^T_{\mathbf{x}'}(\hat{\mathbf{x}}_j)[\sum_{i \in P_j} e_i \nabla I_1^T(\mathbf{x}'_i)] = -\sum_j \mathbf{J}^T_{\mathbf{x}'}(\hat{\mathbf{x}}_j)\mathbf{b}_j, \tag{9.51}$$

where $\hat{\mathbf{x}}_j$ is the *center* of each patch P_j (Shum and Szeliski 2000). This is equivalent to replacing the true motion Jacobian with a piecewise-constant approximation. In practice, this works quite well.

Compositional approach. For a complex parametric motion such as a homography, the computation of the motion Jacobian becomes complicated and may involve a per-pixel division. Szeliski and Shum (1997) observed that this can be simplified by first warping the target image I_1 according to the current motion estimate $\mathbf{x}'(\mathbf{x};\mathbf{p})$,

$$\tilde{I}_1(\mathbf{x}) = I_1(\mathbf{x}'(\mathbf{x};\mathbf{p})), \tag{9.52}$$

and then comparing this *warped* image against the template $I_0(\mathbf{x})$. Subsequently Hager and Belhumeur (1998) suggested replacing the gradient of $\tilde{I}_1(\mathbf{x})$ with the gradient of $I_0(\mathbf{x})$, as described previously in (9.36), which allows the precomputation (and inversion) of the Hessian matrix $\mathbf{A}$ given in (9.46). The residual vector $\mathbf{b}$ (9.47) can also be partially precomputed, i.e., the *steepest descent* images $\nabla I_0(\mathbf{x})\mathbf{J}_{\tilde{\mathbf{x}}}(\mathbf{x})$ can be precomputed and stored for later multiplication with the $e(\mathbf{x}) = \tilde{I}_1(\mathbf{x}) - I_0(\mathbf{x})$ error images, as described in (Szeliski 2010, Section 8.2) and (Baker and Matthews 2004), where this is called the *inverse additive* scheme. Baker and Matthews (2004) also introduce one more variant they call the *inverse compositional* algorithm where they warp the template image $I_0(\mathbf{x})$ and precompute the inverse Hessian and the steepest descent images, which makes it the preferred approach. They also discuss the advantage of using Gauss–Newton iteration (i.e., the first-order expansion of the least squares, as above) compared to other approaches such as steepest descent and Levenberg–Marquardt.

Subsequent parts of the series (Baker, Gross *et al.* 2003; Baker, Gross, and Matthews 2003, 2004) discuss more advanced topics such as per-pixel weighting, pixel selection for efficiency, a more in-depth discussion of robust metrics and algorithms, linear appearance variations, and priors on parameters. They make for invaluable reading for anyone interested in implementing a highly tuned implementation of incremental image registration and have been widely used as components of subsequent object trackers, which are discussed in Section 9.4.4. Evangelidis and Psarakis (2008) provide some detailed experimental evaluations of these and other related approaches.

Learned motion models

An alternative to parameterizing the motion field with a geometric deformation such as an affine transform is to learn a set of basis functions tailored to a particular application (Black, Yacoob *et al.* 1997). First, a set of dense motion fields (Section 9.3) is computed from a set of training videos. Next, singular value decomposition (SVD) is applied to the stack of motion fields $\mathbf{u}_t(\mathbf{x})$ to compute the first few singular vectors $\mathbf{v}_k(\mathbf{x})$. Finally, for a new test sequence, a novel flow field is computed using a coarse-to-fine algorithm that estimates the unknown coefficient a_k in the parameterized flow field

$$\mathbf{u}(\mathbf{x}) = \sum_k a_k \mathbf{v}_k(\mathbf{x}). \tag{9.53}$$

Figure 9.3a shows a set of basis fields learned by observing videos of walking motions. Figure 9.3b shows the temporal evolution of the basis coefficients as well as a few of the recovered parametric motion fields. Note that similar ideas can also be applied to feature tracks (Torresani, Hertzmann, and Bregler 2008), which is a topic we discuss in more detail in Sections 7.1.5 and 13.6.4, as well as video stabilization (Yu and Ramamoorthi 2020).

9.2.1 *Application*: Video stabilization

Video stabilization is one of the most widely used applications of parametric motion estimation (Hansen, Anandan *et al.* 1994; Irani, Rousso, and Peleg 1997; Morimoto and Chellappa 1997; Srinivasan, Chellappa *et al.* 2005; Grundmann, Kwatra, and Essa 2011). Algorithms for stabilization

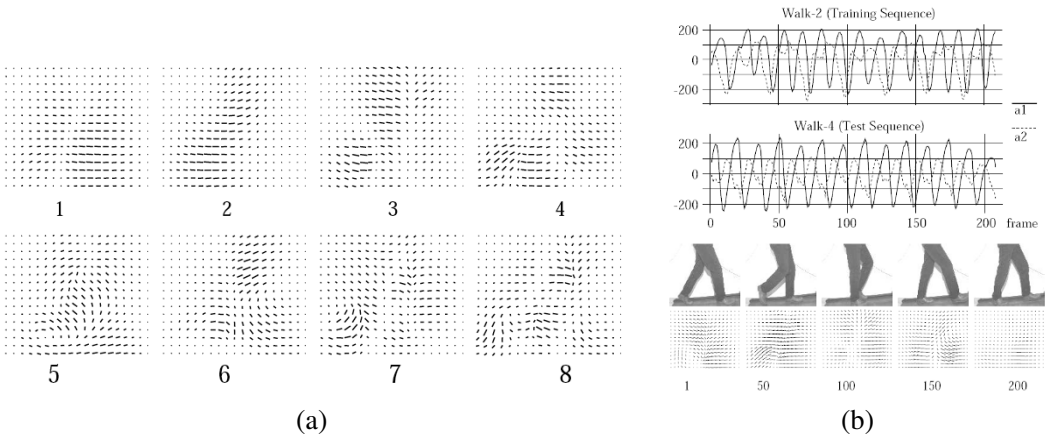

Figure 9.3 Learned parameterized motion fields for a walking sequence (Black, Yacoob *et al.* 1997) © 1997 IEEE: (a) learned basis flow fields; (b) plots of motion coefficients over time and corresponding estimated motion fields.

run inside both hardware devices, such as camcorders and still cameras, and software packages for improving the visual quality of shaky videos.

In their paper on full-frame video stabilization, Matsushita, Ofek *et al.* (2006) give a nice overview of the three major stages of stabilization, namely motion estimation, motion smoothing, and image warping. Motion estimation algorithms often use a similarity transform to handle camera translations, rotations, and zooming. The tricky part is getting these algorithms to lock onto the background motion, which is a result of the camera movement, without getting distracted by independently moving foreground objects (Yu and Ramamoorthi 2018, 2020; Yu, Ramamoorthi *et al.* 2021). Motion smoothing algorithms recover the low-frequency (slowly varying) part of the motion and then estimate the high-frequency shake component that needs to be removed. While quadratic penalties on motion derivatives are commonly used, more realistic virtual camera motions (locked and linear) can be obtained using L_1 minimization of derivatives (Grundmann, Kwatra, and Essa 2011). Finally, image warping algorithms apply the high-frequency correction to render the original frames as if the camera had undergone only the smooth motion.

The resulting stabilization algorithms can greatly improve the appearance of shaky videos but they often still contain visual artifacts. For example, image warping can result in missing borders around the image, which must be cropped, filled using information from other frames, or hallucinated using inpainting techniques (Section 10.5.1). Furthermore, video frames captured during fast motion are often blurry. Their appearance can be improved either by using deblurring techniques (Section 10.3) or by stealing sharper pixels from other frames with less motion or better focus (Matsushita, Ofek *et al.* 2006). Exercise 9.3 has you implement and test some of these ideas.

In situations where the camera is translating a lot in 3D, e.g., when the videographer is walking, an even better approach is to compute a full structure from motion reconstruction of the camera motion and 3D scene. One or more smooth 3D camera paths can then be computed and the original video re-rendered using view interpolation with the interpolated 3D point cloud serving as the proxy geometry while preserving salient features in what is sometimes called *content preserving warps* (Liu, Gleicher *et al.* 2009, 2011; Liu, Yuan *et al.* 2013; Kopf, Cohen, and Szeliski 2014). If you have access to a camera array instead of a single video camera, you can do even better using a light field rendering approach (Section 14.3) (Smith, Zhang *et al.* 2009).

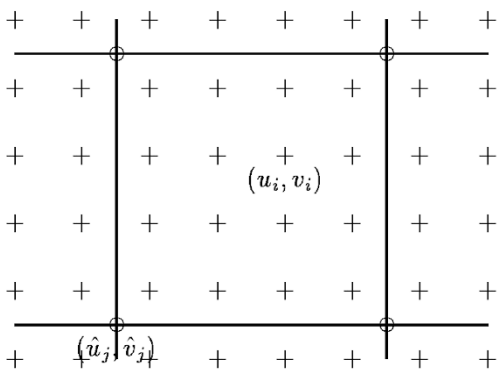

Figure 9.4 Spline motion field: the displacement vectors $\mathbf{u}_i = (u_i, v_i)$ are shown as pluses (+) and are controlled by the smaller number of control vertices $\hat{\mathbf{u}}_j = (\hat{u}_i, \hat{v}_j)$, which are shown as circles (○).

9.2.2 Spline-based motion

While parametric motion models are useful in a wide variety of applications (such as video stabilization and mapping onto planar surfaces), most image motion is too complicated to be captured by such low-dimensional models.

Traditionally, optical flow algorithms (Section 9.3) compute an independent motion estimate for each pixel, i.e., the number of flow vectors computed is equal to the number of input pixels. The general optical flow analog to Equation (9.1) can thus be written as

$$E_{\text{SSD-OF}}(\{\mathbf{u}_i\}) = \sum_i [I_1(\mathbf{x}_i + \mathbf{u}_i) - I_0(\mathbf{x}_i)]^2. \tag{9.54}$$

Notice how in the above equation, the number of variables $\{\mathbf{u}_i\}$ is twice the number of measurements, so the problem is underconstrained.

The two classic approaches to this problem, which we study in Section 9.3, are to perform the summation over overlapping regions (the *patch-based* or *window-based* approach) or to add smoothness terms on the $\{\mathbf{u}_i\}$ field using *regularization* or *Markov random fields* (Chapter 4). In this section, we describe an alternative approach that lies somewhere between general optical flow (independent flow at each pixel) and parametric flow (a small number of global parameters). The approach is to represent the motion field as a two-dimensional *spline* controlled by a smaller number of *control vertices* $\{\hat{\mathbf{u}}_j\}$ (Figure 9.4),

$$\mathbf{u}_i = \sum_j \hat{\mathbf{u}}_j B_j(\mathbf{x}_i) = \sum_j \hat{\mathbf{u}}_j w_{i,j}, \tag{9.55}$$

where the $B_j(\mathbf{x}_i)$ are called the *basis functions* and are only non-zero over a small *finite support* interval (Szeliski and Coughlan 1997). We call the $w_{ij} = B_j(\mathbf{x}_i)$ *weights* to emphasize that the $\{\mathbf{u}_i\}$ are known linear combinations of the $\{\hat{\mathbf{u}}_j\}$.

Substituting the formula for the individual per-pixel flow vectors $\mathbf{u}_i$ (9.55) into the SSD error metric (9.54) yields a parametric motion formula similar to Equation (9.43). The biggest difference is that the Jacobian $\mathbf{J}_1(\mathbf{x}'_i)$ (9.45) now consists of the sparse entries in the weight matrix $\mathbf{W} = [w_{ij}]$.

In situations where we know something more about the motion field, e.g., when the motion is due to a camera moving in a static scene, we can use more specialized motion models. For example, the *plane plus parallax* model (Section 2.1.4) can be naturally combined with a spline-based motion

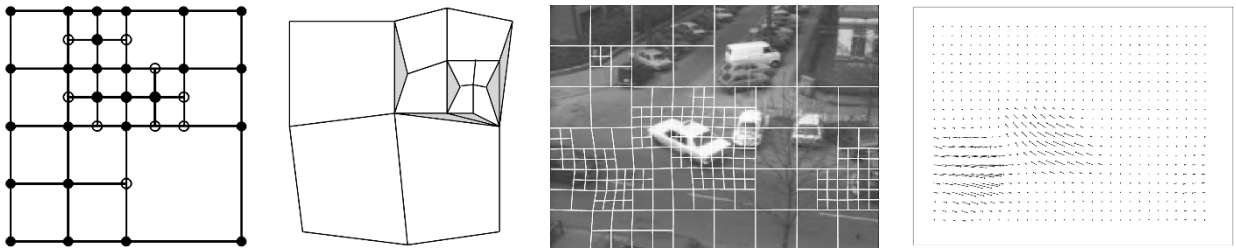

(a) (b) (c) (d)

Figure 9.5 Quadtree spline-based motion estimation (Szeliski and Shum 1996) © 1996 IEEE: (a) quadtree spline representation, (b) which can lead to *cracks*, unless the white nodes are constrained to depend on their parents; (c) deformed quadtree spline mesh overlaid on grayscale image; (d) flow field visualized as a needle diagram.

representation, where the in-plane motion is represented by a homography (8.19) and the out-of-plane parallax d is represented by a scalar variable at each spline control point (Szeliski and Kang 1995; Szeliski and Coughlan 1997).

In many cases, the small number of spline vertices results in a motion estimation problem that is well conditioned. However, if large textureless regions (or elongated edges subject to the aperture problem) persist across several spline patches, it may be necessary to add a *regularization* term to make the problem well posed (Section 4.2). The simplest way to do this is to directly add squared difference penalties between adjacent vertices in the spline control mesh $\{\hat{\mathbf{u}}_j\}$, as in (4.24). If a multi-resolution (coarse-to-fine) strategy is being used, it is important to re-scale these smoothness terms while going from level to level.

The linear system corresponding to the spline-based motion estimator is sparse and regular. Because it is usually of moderate size, it can often be solved using direct techniques such as Cholesky decomposition (Appendix A.4). Alternatively, if the problem becomes too large and subject to excessive fill-in, iterative techniques such as hierarchically preconditioned conjugate gradient (Szeliski 1990b, 2006b; Krishnan and Szeliski 2011; Krishnan, Fattal, and Szeliski 2013) can be used instead (Appendix A.5).

Because of its robustness, spline-based motion estimation has been used for a number of applications, including visual effects (Roble 1999) and medical image registration (Section 9.2.3) (Szeliski and Lavallée 1996; Kybic and Unser 2003).

One disadvantage of the basic technique, however, is that the model does a poor job near motion discontinuities, unless an excessive number of nodes are used. To remedy this situation, Szeliski and Shum (1996) propose using a *quadtree* representation embedded in the spline control grid (Figure 9.5a). Large cells are used to present regions of smooth motion, while smaller cells are added in regions of motion discontinuities (Figure 9.5c).

To estimate the motion, a coarse-to-fine strategy is used. Starting with a regular spline imposed over a lower-resolution image, an initial motion estimate is obtained. Spline patches where the motion is inconsistent, i.e., the squared residual (9.54) is above a threshold, are subdivided into smaller patches. To avoid *cracks* in the resulting motion field (Figure 9.5b), the values of certain nodes in the refined mesh, i.e., those adjacent to larger cells, need to be *restricted* so that they depend on their parent values. This is most easily accomplished using a hierarchical basis representation for the quadtree spline (Szeliski 1990b) and selectively setting some of the hierarchical basis functions to 0, as described in (Szeliski and Shum 1996).

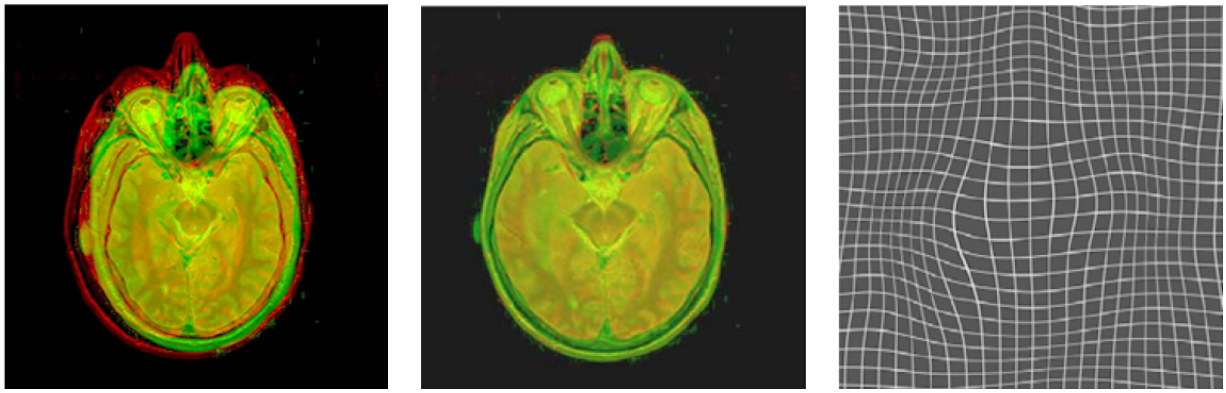

(a) (b) (c)

Figure 9.6 Elastic brain registration (Kybic and Unser 2003) © 2003 IEEE: (a) original brain atlas and patient MRI images overlaid in red–green; (b) after elastic registration with eight user-specified landmarks (not shown); (c) a cubic B-spline deformation field, shown as a deformed grid.

9.2.3 *Application*: Medical image registration

Because they excel at representing smooth *elastic* deformation fields, spline-based motion models have found widespread use in medical image registration (Bajcsy and Kovacic 1989; Szeliski and Lavallée 1996; Christensen, Joshi, and Miller 1997).[10] Registration techniques can be used both to track an individual patient's development or progress over time (a *longitudinal* study) or to match different patient images together to find commonalities and detect variations or pathologies (*cross-sectional* studies). When different imaging *modalities* are being registered, e.g., computed tomography (CT) scans and magnetic resonance images (MRI), *mutual information* measures of similarity are often necessary (Viola and Wells III 1997; Maes, Collignon *et al.* 1997).

Kybic and Unser (2003) provide a nice literature review and describe a complete working system based on representing both the images and the deformation fields as multi-resolution splines. Figure 9.6 shows an example of the Kybic and Unser system being used to register a patient's brain MRI with a labeled brain atlas image. The system can be run in a fully automatic mode but more accurate results can be obtained by locating a few key *landmarks*. More recent papers on deformable medical image registration, including performance evaluations, include Klein, Staring, and Pluim (2007), Glocker, Komodakis *et al.* (2008), and the survey by Sotiras, Davatzikos, and Paragios (2013).

As with other applications, regular volumetric splines can be enhanced using selective refinement. In the case of 3D volumetric image or surface registration, these are known as *octree splines* (Szeliski and Lavallée 1996) and have been used to register medical surface models such as vertebrae and faces from different patients (Figure 9.7).

9.3 Optical flow

The most general (and challenging) version of motion estimation is to compute an independent estimate of motion at *each* pixel, which is generally known as *optical* (or *optic*) *flow*. As we mentioned in the previous section, this generally involves minimizing the brightness or color difference between

[10] In computer graphics, such elastic volumetric deformations are known as *free-form deformations* (Sederberg and Parry 1986; Coquillart 1990; Celniker and Gossard 1991).

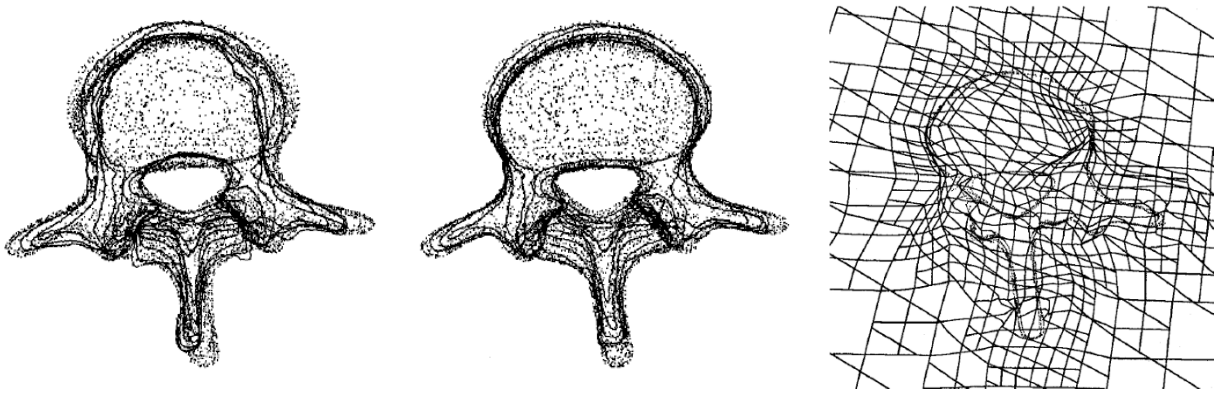

(a) (b) (c)

Figure 9.7 Octree spline-based image registration of two vertebral surface models (Szeliski and Lavallée 1996) © 1996 Springer: (a) after initial rigid alignment; (b) after elastic alignment; (c) a cross-section through the adapted octree spline deformation field.

corresponding pixels summed over the image,

$$E_{\text{SSD-OF}}(\{\mathbf{u}_i\}) = \sum_i [I_1(\mathbf{x}_i + \mathbf{u}_i) - I_0(\mathbf{x}_i)]^2. \tag{9.56}$$

Because the number of variables $\{\mathbf{u}_i\}$ is twice the number of measurements, the problem is under-constrained. The two classic approaches to this problem are to perform the summation *locally* over overlapping regions (the *patch-based* or *window-based* approach) or to add smoothness terms on the $\{\mathbf{u}_i\}$ field using regularization or Markov random fields (Chapter 4) and to search for a global minimum. Good overviews of recent optical flow algorithms can be found in Baker, Scharstein *et al.* (2011), Sun, Yang *et al.* (2018), Janai, Güney *et al.* (2020), and Hur and Roth (2020).

The patch-based approach usually involves using a Taylor series expansion of the displaced image function (9.28) to obtain sub-pixel estimates (Lucas and Kanade 1981). Anandan (1989) shows how a series of local discrete search steps can be interleaved with Lucas–Kanade incremental refinement steps in a coarse-to-fine pyramid scheme, which allows the estimation of large motions, as described in Section 9.1.1. He also analyzes how the *uncertainty* in local motion estimates is related to the eigenvalues of the local Hessian matrix $\mathbf{A}_i$ (9.37), as shown in Figures 7.4 and 7.5.

Bergen, Anandan *et al.* (1992) develop a unified framework for describing both parametric (Section 9.2) and patch-based optical flow algorithms and provide a nice introduction to this topic. After each iteration of optical flow estimation in a coarse-to-fine pyramid, they re-warp one of the images so that only incremental flow estimates are computed (Section 9.1.1). When overlapping patches are used, an efficient implementation is to first compute the outer products of the gradients and intensity errors (9.33–9.34) at every pixel and then perform the overlapping window sums using a moving average filter.[11]

Instead of solving for each motion (or motion update) independently, Horn and Schunck (1981) develop a regularization-based framework where (9.56) is simultaneously minimized over all flow vectors $\{\mathbf{u}_i\}$. To constrain the problem, smoothness constraints, i.e., squared penalties on flow derivatives, are added to the basic per-pixel error metric. Because the technique was originally developed for small motions in a variational (continuous function) framework, the linearized *brightness constancy constraint* corresponding to (9.28), i.e., (9.31), is more commonly written as an

[11] Other smoothing or aggregation filters can also be used at this stage (Bruhn, Weickert, and Schnörr 2005).

analytic integral

$$E_{\mathrm{HS}} = \int (I_x u + I_y v + I_t)^2 \, dx \, dy, \tag{9.57}$$

where $(I_x, I_y) = \nabla I_1 = \mathbf{J}_1$, $I_t = e_i$ is the *temporal derivative*, i.e., the brightness change between images, and $u(x, y)$ and $v(x, y)$ are the 2D optical flow functions. The Horn and Schunck model can also be viewed as the limiting case of spline-based motion estimation as the splines become 1×1 pixel patches.

It is also possible to combine ideas from local and global flow estimation into a single framework by using a locally aggregated (as opposed to single-pixel) Hessian as the brightness constancy term (Bruhn, Weickert, and Schnörr 2005). Consider the discrete analog (9.28) to the analytic global energy (9.57),

$$E_{\mathrm{HSD}} = \sum_i \mathbf{u}_i^T [\mathbf{J}_i \mathbf{J}_i^T] \mathbf{u}_i + 2 e_i \mathbf{J}_i^T \mathbf{u}_i + e_i^2. \tag{9.58}$$

If we replace the per-pixel (rank 1) Hessians $\mathbf{A}_i = [\mathbf{J}_i \mathbf{J}_i^T]$ and residuals $\mathbf{b}_i = \mathbf{J}_i e_i$ with area-aggregated versions (9.33–9.34), we obtain a global minimization algorithm where region-based brightness constraints are used.

Another extension to the basic optical flow model is to use a combination of global (parametric) and local motion models. For example, if we know that the motion is due to a camera moving in a static scene (rigid motion), we can re-formulate the problem as the estimation of a per-pixel depth along with the parameters of the global camera motion (Adiv 1989; Hanna 1991; Bergen, Anandan *et al.* 1992; Szeliski and Coughlan 1997; Nir, Bruckstein, and Kimmel 2008; Wedel, Cremers *et al.* 2009). Such techniques are closely related to stereo matching (Chapter 12). Alternatively, we can estimate either per-image or per-segment affine motion models combined with per-pixel *residual* corrections (Black and Jepson 1996; Ju, Black, and Jepson 1996; Chang, Tekalp, and Sezan 1997; Mémin and Pérez 2002). We revisit this topic in Section 9.4.

Of course, image brightness may not always be an appropriate metric for measuring appearance consistency, e.g., when the lighting in an image is varying. As discussed in Section 9.1, matching gradients, filtered images, or other metrics such as image Hessians (second derivative measures) may be more appropriate. It is also possible to locally compute the *phase* of steerable filters in the image, which is insensitive to both bias and gain transformations (Fleet and Jepson 1990). Papenberg, Bruhn *et al.* (2006) review and explore such constraints and also provide a detailed analysis and justification for iteratively re-warping images during incremental flow computation.

Because the brightness constancy constraint is evaluated at each pixel independently, rather than being summed over patches where the constant flow assumption may be violated, global optimization approaches tend to perform better near motion discontinuities. This is especially true if robust metrics are used in the smoothness constraint (Black and Anandan 1996; Bab-Hadiashar and Suter 1998a).[12] One popular choice for robust metrics is the L_1 norm, also known as *total variation* (TV), which results in a convex energy whose global minimum can be found (Bruhn, Weickert, and Schnörr 2005; Papenberg, Bruhn *et al.* 2006; Zach, Pock, and Bischof 2007b; Zimmer, Bruhn, and Weickert 2011). Anisotropic smoothness priors, which apply a different smoothness in the directions parallel and perpendicular to the image gradient, are another popular choice (Nagel and Enkelmann 1986; Sun, Roth *et al.* 2008; Werlberger, Trobin *et al.* 2009; Werlberger, Pock, and Bischof 2010). It is also possible to learn a set of better smoothness constraints (derivative filters and robust functions) from a set of paired flow and intensity images (Sun, Roth *et al.* 2008). Many of these techniques are discussed in more detail by Baker, Scharstein *et al.* (2011) and Sun, Roth, and Black (2014).

[12] Robust brightness metrics (Section 9.1, (9.2)) can also help improve the performance of window-based approaches (Black and Anandan 1996).

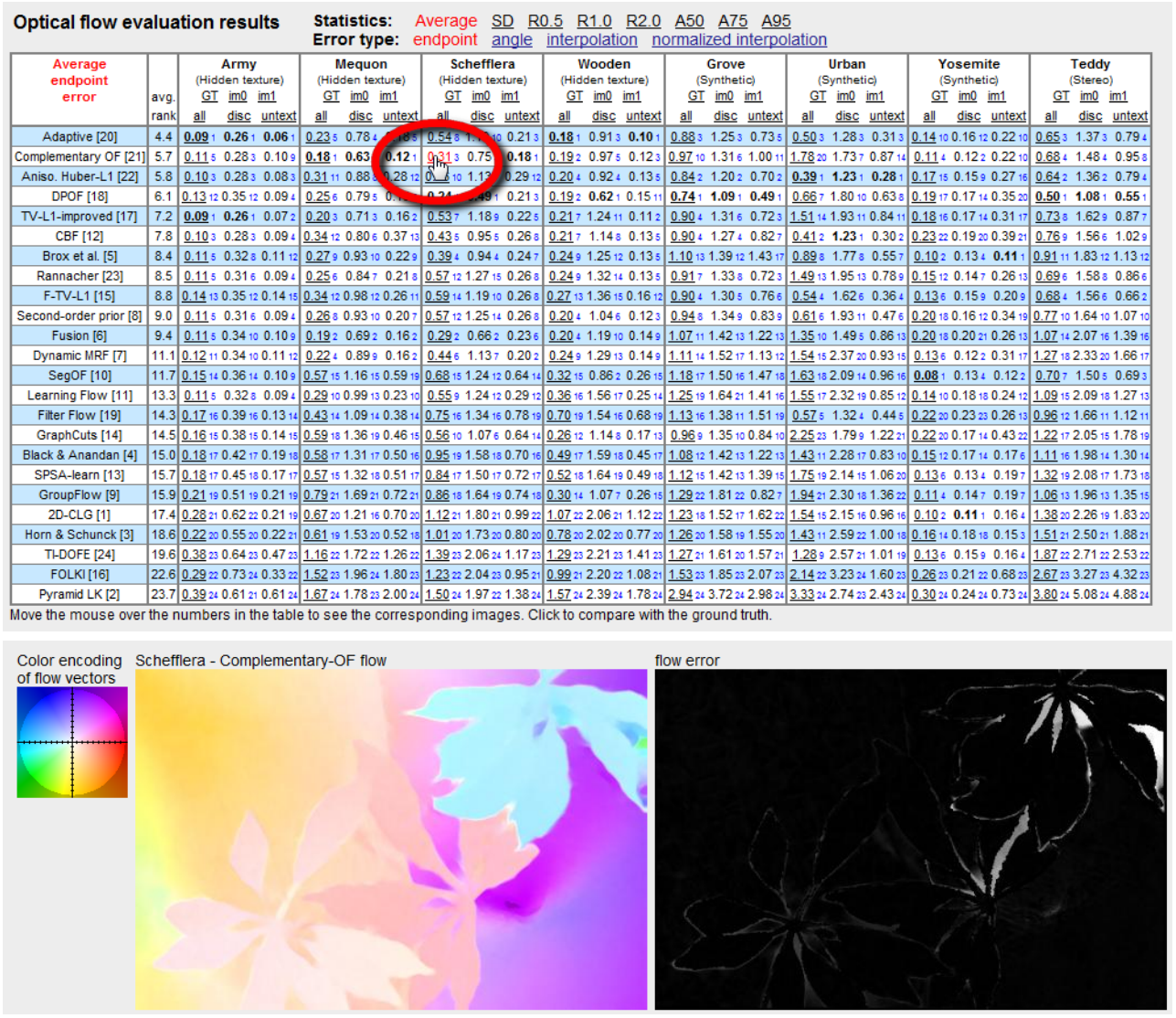

Optical flow evaluation results

Statistics: Average SD R0.5 R1.0 R2.0 A50 A75 A95
Error type: endpoint angle interpolation normalized interpolation

Average endpoint error	avg. rank	Army (Hidden texture) GT im0 im1 all	disc	untext	Mequon (Hidden texture) GT im0 im1 all	disc	untext	Schefflera (Hidden texture) GT im0 im1 all	disc	untext	Wooden (Hidden texture) GT im0 im1 all	disc	untext	Grove (Synthetic) GT im0 im1 all	disc	untext	Urban (Synthetic) GT im0 im1 all	disc	untext	Yosemite (Synthetic) GT im0 im1 all	disc	untext	Teddy (Stereo) GT im0 im1 all	disc	untext
Adaptive [20]	4.4	**0.09** 1	**0.26** 1	**0.06** 1	0.23 5	0.78 4	0.18 3	0.54 8	1.10 10	0.21 3	**0.18** 1	0.91 3	**0.10** 1	0.88 3	1.25 3	0.73 5	0.50 3	1.28 3	0.31 3	0.14 10	0.16 12	0.22 10	0.65 3	1.37 3	0.79 4
Complementary OF [21]	5.7	0.11 5	0.28 3	0.10 9	**0.18** 1	**0.63** 1	**0.12** 1	0.31 3	0.75 3	**0.18** 1	0.19 2	0.97 5	0.12 3	0.97 10	1.31 6	1.00 11	1.78 20	1.73 7	0.87 14	0.11 4	0.12 2	0.22 10	0.68 4	1.48 4	0.95 8
Aniso. Huber-L1 [22]	5.8	0.10 3	0.28 3	0.08 3	0.31 11	0.88 9	0.28 12	0.42 10	1.13 9	0.29 12	0.20 4	0.92 4	0.13 5	0.84 2	1.20 2	0.70 2	**0.39** 1	**1.23** 1	**0.28** 1	0.17 15	0.15 9	0.27 16	0.64 2	1.36 2	0.79 4
DPOF [18]	6.1	0.13 12	0.35 12	0.09 4	0.25 6	0.79 5	0.17 2	0.24 1	0.49 1	0.21 3	0.19 2	**0.62** 1	0.15 11	**0.74** 1	**1.09** 1	**0.49** 1	0.66 7	1.80 10	0.63 8	0.19 17	0.17 14	0.35 20	**0.50** 1	**1.08** 1	**0.55** 1
TV-L1-improved [17]	7.2	**0.09** 1	**0.26** 1	0.07 2	0.20 3	0.71 3	0.16 2	0.53 7	1.18 9	0.22 5	0.21 7	1.24 11	0.11 2	0.90 4	1.31 6	0.72 3	1.51 14	1.93 11	0.84 11	0.18 16	0.17 14	0.31 17	0.73 8	1.62 9	0.87 7
CBF [12]	7.8	0.10 3	0.28 3	0.09 4	0.34 12	0.80 6	0.37 13	0.43 5	0.95 5	0.26 8	0.21 7	1.14 8	0.13 5	0.90 4	1.27 4	0.82 7	0.41 2	**1.23** 1	0.30 2	0.23 22	0.19 20	0.39 21	0.76 9	1.56 6	1.02 9
Brox et al. [5]	8.4	0.11 5	0.32 8	0.11 12	0.27 9	0.93 10	0.22 9	0.39 4	0.94 4	0.24 7	0.24 9	1.25 12	0.13 5	1.10 13	1.39 12	1.43 17	0.89 8	1.77 8	0.55 7	0.10 2	0.13 4	**0.11** 1	0.91 11	1.83 12	1.13 12
Rannacher [23]	8.5	0.11 5	0.31 6	0.09 4	0.25 6	0.84 7	0.21 8	0.57 12	1.27 15	0.26 8	0.24 9	1.32 14	0.13 5	0.91 7	1.33 8	0.72 3	1.49 13	1.95 13	0.78 9	0.15 12	0.14 7	0.26 13	0.69 6	1.58 8	0.86 6
F-TV-L1 [15]	8.8	0.14 13	0.35 12	0.14 15	0.34 12	0.98 12	0.26 11	0.59 14	1.19 10	0.26 8	0.27 13	1.36 15	0.16 12	0.90 4	1.30 5	0.76 6	0.54 4	1.62 6	0.36 4	0.13 6	0.15 9	0.20 9	0.68 4	1.56 6	0.66 2
Second-order prior [8]	9.0	0.11 5	0.31 6	0.09 4	0.26 8	0.93 10	0.20 7	0.57 12	1.25 14	0.26 8	0.20 4	1.04 6	0.12 3	0.94 8	1.34 9	0.83 9	0.61 6	1.93 11	0.47 6	0.20 18	0.16 12	0.34 19	0.77 10	1.64 10	1.07 10
Fusion [6]	9.4	0.11 5	0.34 10	0.10 9	0.19 2	0.69 2	0.16 2	0.29 2	0.66 2	0.23 6	0.20 4	1.19 10	0.14 9	1.07 11	1.42 13	1.22 13	1.35 10	1.49 5	0.86 13	0.20 18	0.20 21	0.26 13	1.07 14	2.07 16	1.39 16
Dynamic MRF [7]	11.1	0.12 11	0.34 10	0.11 12	0.22 4	0.89 9	0.16 2	0.44 6	1.13 7	0.20 2	0.24 9	1.29 13	0.14 9	1.11 14	1.52 17	1.13 12	1.54 15	2.37 20	0.93 15	0.13 6	0.12 2	0.31 17	1.27 18	2.33 20	1.66 17
SegOF [10]	11.7	0.15 14	0.36 14	0.10 9	0.57 15	1.16 15	0.59 19	0.68 15	1.24 12	0.64 14	0.32 15	0.86 2	0.26 15	1.18 17	1.50 16	1.47 18	1.63 18	2.09 14	0.96 16	**0.08** 1	0.13 4	0.12 2	0.70 7	1.50 5	0.69 3
Learning Flow [11]	13.3	0.11 5	0.32 8	0.09 4	0.29 10	0.99 13	0.23 10	0.55 9	1.24 12	0.29 12	0.36 16	1.56 17	0.25 14	1.25 19	1.64 21	1.41 16	1.55 17	2.32 19	0.85 12	0.14 10	0.18 18	0.24 12	1.09 15	2.09 18	1.27 13
Filter Flow [19]	14.3	0.17 16	0.39 16	0.13 14	0.43 14	1.09 14	0.38 14	0.75 16	1.34 16	0.78 19	0.70 19	1.54 16	0.68 19	1.13 16	1.38 11	1.51 19	0.57 5	1.32 4	0.44 5	0.22 20	0.23 23	0.26 13	0.96 12	1.66 11	1.12 11
GraphCuts [14]	14.5	0.16 15	0.38 15	0.14 15	0.59 18	1.36 19	0.46 15	0.56 10	1.07 6	0.64 14	0.26 12	1.14 8	0.17 13	0.96 9	1.35 10	0.84 10	2.25 23	1.79 9	1.22 21	0.22 20	0.17 14	0.43 22	1.22 17	2.05 15	1.78 19
Black & Anandan [4]	15.0	0.18 17	0.42 17	0.19 18	0.58 17	1.31 17	0.50 16	0.95 19	1.58 18	0.70 16	0.49 17	1.59 18	0.45 17	1.08 12	1.42 13	1.22 13	1.43 11	2.28 17	0.83 10	0.15 12	0.17 14	0.17 6	1.11 16	1.98 14	1.30 14
SPSA-learn [13]	15.7	0.18 17	0.45 18	0.17 17	0.57 15	1.32 18	0.51 17	0.84 17	1.50 17	0.72 17	0.52 18	1.64 19	0.49 18	1.12 15	1.42 13	1.39 15	1.75 19	2.14 15	1.06 20	0.13 6	0.13 4	0.19 7	1.32 19	2.08 17	1.73 18
GroupFlow [9]	15.9	0.21 19	0.51 19	0.21 19	0.79 21	1.69 21	0.72 21	0.86 18	1.64 19	0.74 18	0.30 14	1.07 7	0.26 15	1.29 22	1.81 22	0.82 7	1.94 21	2.30 18	1.36 22	0.11 4	0.14 7	0.19 7	1.06 13	1.96 13	1.35 15
2D-CLG [1]	17.4	0.28 21	0.62 22	0.21 19	0.67 20	1.21 16	0.70 20	1.12 21	1.80 21	0.99 22	1.07 22	2.06 21	1.12 22	1.23 18	1.52 17	1.62 22	1.54 15	2.15 16	0.96 16	0.10 2	**0.11** 1	0.16 4	1.38 20	2.26 19	1.83 20
Horn & Schunck [3]	18.6	0.22 20	0.55 20	0.22 21	0.61 19	1.53 20	0.52 18	1.01 20	1.73 20	0.80 20	0.78 20	2.02 20	0.77 20	1.26 20	1.58 19	1.55 20	1.43 11	2.59 22	1.00 18	0.16 14	0.18 18	0.15 3	1.51 21	2.50 21	1.88 21
TI-DOFE [24]	19.6	0.38 23	0.64 23	0.47 23	1.16 22	1.72 22	1.26 22	1.39 23	2.06 24	1.17 23	1.29 23	2.21 23	1.41 23	1.27 21	1.61 20	1.57 21	1.28 9	2.57 21	1.01 19	0.13 6	0.15 9	0.16 4	1.87 22	2.71 22	2.53 22
FOLKI [16]	22.6	0.29 22	0.73 24	0.33 22	1.52 23	1.96 24	1.80 23	1.23 22	2.04 23	0.95 21	0.99 21	2.20 22	1.08 21	1.53 23	1.85 23	2.07 23	2.14 22	3.23 24	1.60 23	0.26 23	0.21 22	0.68 23	2.67 23	3.27 23	4.32 23
Pyramid LK [2]	23.7	0.39 24	0.61 21	0.61 24	1.67 24	1.78 23	2.00 24	1.50 24	1.97 22	1.38 24	1.57 24	2.39 24	1.78 24	2.94 24	3.72 24	2.98 24	3.33 24	2.74 23	2.43 24	0.30 24	0.24 24	0.73 24	3.80 24	5.08 24	4.88 24

Move the mouse over the numbers in the table to see the corresponding images. Click to compare with the ground truth.

Figure 9.8 Evaluation of the results of 24 optical flow algorithms, October 2009, https://vision.middlebury.edu/flow, (Baker, Scharstein *et al.* 2009). By moving the mouse pointer over an underlined performance score, the user can interactively view the corresponding flow and error maps. Clicking on a score toggles between the computed and ground truth flows. Next to each score, the corresponding rank in the current column is indicated by a smaller blue number. The minimum (best) score in each column is shown in boldface. The table is sorted by the average rank (computed over all 24 columns, three region masks for each of the eight sequences). The average rank serves as an *approximate* measure of performance *under the selected metric/statistic*.

Because of the large, two-dimensional search space in estimating flow, most algorithms use variations of gradient descent and coarse-to-fine continuation methods to minimize the global energy function. This contrasts starkly with stereo matching, which is an "easier" one-dimensional disparity estimation problem, where combinatorial optimization techniques were the method of choice until the advent of deep neural networks.[13] One way to deal with this complexity is to start with efficient patch-based correspondences (Kroeger, Timofte *et al.* 2016). Another way to deal with the large two-dimensional search space is to integrate sparse feature matches into a variational formulation, as was initially proposed by Brox and Malik (2010a). This approach was later extended by several authors, including Weinzaepfel, Revaud *et al.* (2013), whose DeepFlow system use a hand-crafted (non-learnt) convolutional network to compute initial quasi-dense correspondences, and Revaud, Weinzaepfel *et al.* (2015), whose EpicFlow system added an edge and occlusion-aware interpolation step before the variational optimization.

Combinatorial optimization methods based on Markov random fields were among the better-performing methods on the optical flow database of Baker, Scharstein *et al.* (2011)[14] when it was originally released, but have now been overtaken by deep neural networks. Examples of such techniques include the one developed by Glocker, Paragios *et al.* (2008), who use a coarse-to-fine strategy with per-pixel 2D uncertainty estimates, which are then used to guide the refinement and search at the next finer level. Lempitsky, Roth, and Rother (2008) use fusion moves (Lempitsky, Rother, and Blake 2007) over proposals generated from basic flow algorithms (Horn and Schunck 1981; Lucas and Kanade 1981) to find good solutions.

A careful empirical analysis of these kinds of "classic" coarse-to-fine energy-minimization approaches is provided in the meticulously executed paper by Sun, Roth, and Black (2014).[15] Figure 9.9a shows the main components of the framework they examine, including an initial warping based on the previous level's flow (or a grid search at the coarsest level), followed by energy minimizing flow updates, and then an optional post-processing step. In their paper, the authors not only review dozens of variational (energy-minimization) approaches developed from the 1980s (Horn and Schunck 1981) through to 2013, but also show that algorithmic details such as median filtering post-processing, often glossed over by previous authors, have a strong influence on the results. In addition to performing their analysis on the Middlebury Flow dataset (Baker, Scharstein *et al.* 2011), they also evaluate on the newer Sintel dataset (Butler, Wulff *et al.* 2012).[16]

The field of accurate motion estimation continues to evolve at a rapid pace, with significant advances in performance occurring every year. While the Middlebury optical flow website (Figure 9.8) continues to be a good source of pointers to high-performing algorithms, more recent publications tend to focus (both training and evaluation) on the MPI Sintel dataset developed by Butler, Wulff *et al.* (2012), some samples of which are shown in Figure 9.1e–f. Some algorithms also train and test on the KITTI flow benchmark (Geiger, Lenz, and Urtasun 2012), although that dataset focuses on video acquired from a driving vehicle. In general, it appears that learning-based algorithms trained on one dataset still have trouble when applied to a different dataset.[17]

[13] Some exceptions to this trend of not exploring the full 4D cost volume can be found in Xu, Ranftl, and Koltun (2017) and Teed and Deng (2020b).

[14] https://vision.middlebury.edu/flow

[15] The earlier conference version of this paper had the eye-catching title of "Secrets of optical flow estimation and their principles" (Sun, Roth, and Black 2010).

[16] http://sintel.is.tue.mpg.de

[17] http://www.robustvision.net

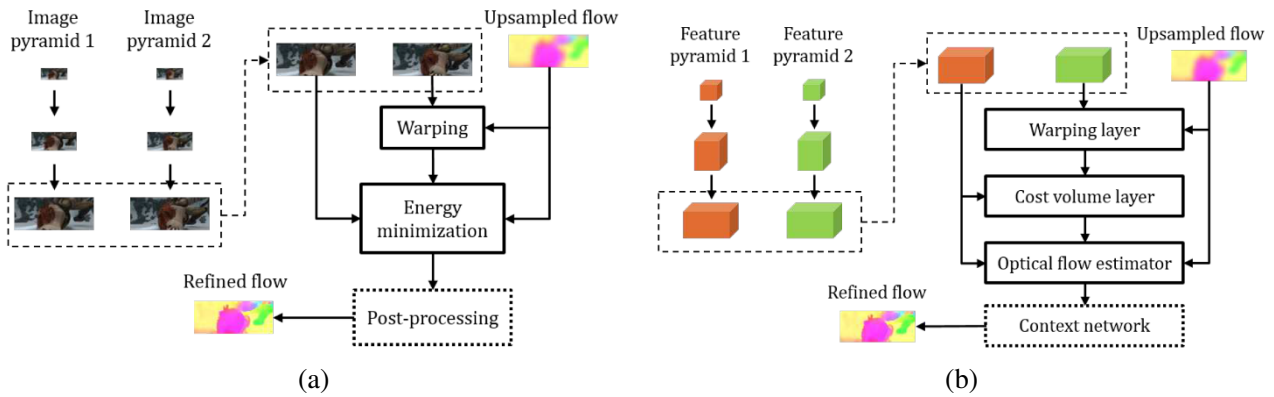

Figure 9.9 Iterative coarse-to-fine optical flow estimation (Sun, Yang *et al.* 2018) © 2018 IEEE: (a) "classic" variational (energy minimization) approach (Sun, Roth, and Black 2014); (b) newer neural network approach trained with end-to-end deep learning (Sun, Yang *et al.* 2018). Both figures show the processing at a *single* level of the coarse-to-fine pyramid, taking as input the flow computed by the previous (coarser) level and passing the refined flow onto the finer level below.

9.3.1 Deep learning approaches

Over the last decade, deep neural networks have become an essential component of all highly-performant optical flow algorithms, as described in the survey articles by Janai, Güney *et al.* (2020, Chapter 11) and Hur and Roth (2020). An early approach to use non-linear aggregation inspired by deep convolutional networks is the DeepFlow system of Weinzaepfel, Revaud *et al.* (2013), which uses a hand-crafted (non-learned) convolutions and pooling to compute multi-level response maps (matching costs), which are then optimized using a classic energy-minimizing variational framework.

The first system to use full deep end-to-end learning in an encoder-decoder network was FlowNetS (Dosovitskiy, Fischer *et al.* 2015), which was trained on the authors' synthetic FlyingChairs dataset. The paper also introduced FlowNetC, which uses a correlation network (local cost volume). The follow-on FlowNet 2.0 system uses the initial flow estimates to warp the images and then refines the flow estimates using cascaded encoder-decoder networks (Ilg, Mayer *et al.* 2017), while subsequent papers also deal with occlusions and uncertainty modeling (Ilg, Saikia *et al.* 2018; Ilg, Çiçek *et al.* 2018).

An alternative to stacking full-resolution networks in series is to use image and flow pyramids together with coarse-to-fine warping and refinement, as first explored in the SPyNet paper by Ranjan and Black (2017). The more recent PWC-Net of Sun, Yang *et al.* (2018, 2019) shown in Figure 9.9b extends this idea by first computing a feature pyramid from each frame, warping the second set of features by the flow interpolated from the previous resolution level, and then computing a cost volume by correlating these features using a dot product between feature maps shifted by up to $d = \pm 4$ pixels. The refined optical flow estimates at the current level are produced using a multi-layer CNN whose inputs are the cost volume, the image features, and the interpolated flow from the previous level. A final context network takes as input the flow estimate and features from the second to last level and uses dilated convolutions to endow the network with a broader context. If you compare Figures 9.9a–b, you will see a pleasing correspondence between the various processing stages of classic and deep coarse-to-fine flow estimation algorithms.[18]

[18] Note that as with other coarse-to-fine warping approaches, these algorithms struggle with fast-moving fine structures that may not be visible at coarser levels (Brox and Malik 2010a).

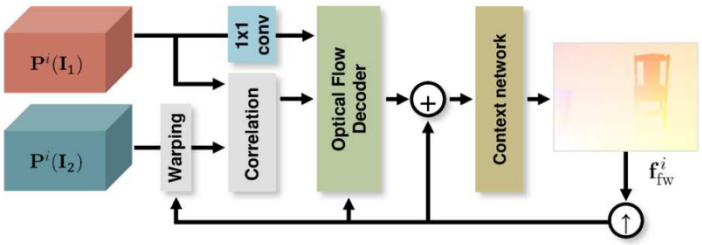

Figure 9.10 Iterative residual refinement optical flow estimation (Hur and Roth 2019) © 2019 IEEE. The coarse-to-fine cascade of Sun, Yang *et al.* (2018) in Figure 9.9b is replaced with a recurrent neural network (RNN) that cycles interpolated coarser level flow estimates as warping inputs to the next finer level but uses the same convolutional weights at each level.

A variant on the coarse-to-fine PWC-Net developed by Hur and Roth (2019) is the Iterative Residual Refinement network shown in Figure 9.10. Instead of cascading a set of different deep networks as in FlowNet 2.0 and PWC-Net, IRRs re-use the same structure and convolution weights at each layer, which allows the network to be re-drawn in the "rolled up" version, as shown in this figure. The network can thus be thought of as a simple recurrent neural network (RNN) that upsamples the output flow estimates after each stage. In addition to having fewer parameters, this weight sharing also improves accuracy. In their paper, the authors also show how this network can be extended (doubled) to simultaneously compute forward and backward flows as well as occlusions.

In more recent work, Jonschkowski, Stone *et al.* (2020) take PWC-Net as their basic architecture and systematically study all of the components involved in training the flow estimator in an *unsupervised* manner, i.e., using regular real-world videos with no ground truth flow, which can enable much larger training sets to be used (Ahmadi and Patras 2016; Meister, Hur, and Roth 2018). In their paper, Jonschkowski *et al.* systematically compare photometric losses, occlusion estimation, self-supervision, and smoothness constraints, and analyze the effect of other choices, such as pre-training, image resolution, data augmentation, and batch size. They also propose four improvements to these key components, including cost volume normalization, gradient stopping for occlusion estimation, applying smoothness at the native flow resolution, and image resizing for self-supervision. Another recent paper that explicitly deals with occlusions is Jiang, Campbell *et al.* (2021).

Another recent trend has been to model the uncertainty that arises in flow field estimation due to homogeneous and occluded regions (Ilg, Çiçek *et al.* 2018). The HD^3 network developed by Yin, Darrell, and Yu (2019) models correspondence distributions across multiple resolution levels, while the LiteFlowNet3 network of Hui and Loy (2020) extends their small and fast LiteFlowNet2 network (Hui, Tang, and Loy 2021) with cost volume modulation and flow field deformation modules to significantly improve accuracy at minimal cost. In concurrent work, Hofinger, Rota Bulò *et al.* (2020) introduce novel components such as replacing warping by sampling, smart gradient blocking, and knowledge distillation, which not only improve the quality of their flow estimates but can also be used in other applications such as stereo matching. Teed and Deng (2020b) build on the idea of a recurrent network (Hur and Roth 2019), but instead of warping feature maps, they precompute a full $(W \times H)^2$ multi-resolution correlation volume (Recurrent All-Pairs Field Transforms or RAFT), which is accessed at each iteration based on the current flow estimates. Computing a sparse correlation volume storing only the k closest matches for each reference image feature can further accelerate the computation (Jiang, Lu *et al.* 2021).

Given the rapid evolution in optical flow techniques, which is the best one to use? The answer is highly problem-dependent. One way to assess this is to look across a number of datasets, as is

done in the Robust Vision Challenge.[19] On this aggregated benchmark, variants of RAFT, IRR, and PWC all perform well. Another is to specifically evaluate a flow algorithm based on its indented use, and, if possible, to fine-tune the network on problem-specific data. Xue, Chen *et al.* (2019) describe how they fine-tune a SPyNet coarse-to-fine network on their synthetically degraded Vimeo-90K dataset to estimate *task-oriented flow* (TOFlow), which outperforms "higher accuracy" networks (and even ground truth flow) on three different video processing tasks, namely frame interpolation (Section 9.4.1), video denoising (Section 9.3.4), and video super-resolution. It is also possible to significantly improve the performance of learning-based flow algorithms by tailoring the synthetic training data to a target dataset (Sun, Vlasic *et al.* 2021).

9.3.2 *Application*: Rolling shutter wobble removal

To save on silicon circuitry and enable greater photo sensitivity or fill factors, many CMOS imaging sensors such as those found in mobile phones use a *rolling shutter*, where different rows or columns are exposed in sequence. When photographing or filming a scene with fast scene or camera motions, this can result in straight lines becoming slanted or curved (e.g., the propeller blades on a plane or helicopter) or rigid parts of the scene wobbling (also known as the *jello effect*), e.g., when the camera is rapidly vibrating during action photography.

To compensate for these distortion, which are caused by different exposure times for different scanlines, accurate per-pixel optical flow must be estimated, as opposed to the whole-frame parametric motion that can sometimes be used for slower-motion video stabilization (Section 9.2.1). Baker, Bennett *et al.* (2010) and Forssén and Ringaby (2010) were among the first computer vision researchers to study this problem. In their paper, Baker, Bennett *et al.* (2010) recover a high-frequency motion field from the lower-frequency inter-frame motions and use this to resample each output scanline. Forssén and Ringaby (2010) perform similar computations using models of camera rotation, which require intrinsic lens calibration. Grundmann, Kwatra *et al.* (2012) remove the need for such calibration using mixtures of homographies to model the camera and scene motions, while Liu, Gleicher *et al.* (2011) use subspace constraints. Accurate rolling shutter correction is also required to produce high-quality image stitching results (Zhuang and Tran 2020).

While in some modern imaging systems such as action cameras, inertial measurements units (IMUs) can provide high-frequency estimates of camera motion, they cannot directly provide estimates of depth-dependent parallax and independent object motions. For this reason, the best in-camera image stabilizers use a combination of IMU data and sophisticated image processing.[20] Modeling rolling shutter is also important to obtain accurate pose estimates in structure from motion (Hedborg, Forssén *et al.* 2012; Kukelova, Albl *et al.* 2018; Albl, Kukelova *et al.* 2020; Kukelova, Albl *et al.* 2020) and visual-inertial fusion in SLAM (Patron-Perez, Lovegrove, and Sibley 2015; Schubert, Demmel *et al.* 2018), which are discussed in Sections 11.4.2 and 11.5.

9.3.3 Multi-frame motion estimation

So far, we have looked at motion estimation as a two-frame problem, where the goal is to compute a motion field that aligns pixels from one image with those in another. In practice, motion estimation is usually applied to video, where a whole sequence of frames is available to perform this task.

One classic approach to multi-frame motion is to *filter* the spatio-temporal volume using oriented or steerable filters (Heeger 1988), in a manner analogous to oriented edge detection (Section 3.2.3). Figure 9.11 shows two frames from the commonly used *flower garden* sequence, as well

[19] http://www.robustvision.net/leaderboard.php?benchmark=flow
[20] https://gopro.com/en/us/news/hero7-black-hypersmooth-technology

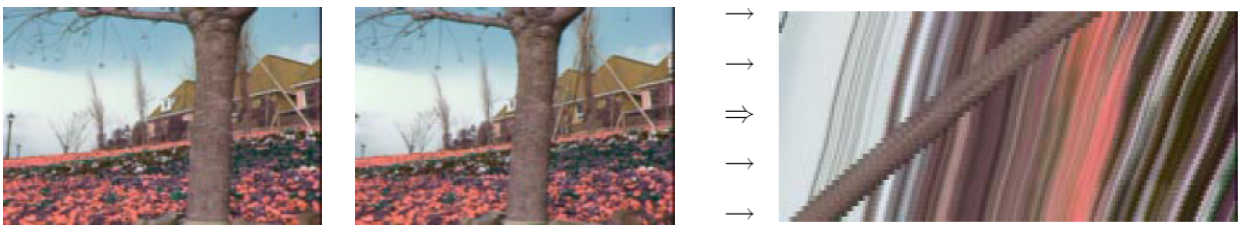

(a) (b) (c)

Figure 9.11 Slice through a spatio-temporal volume (Szeliski 1999a) © 1999 IEEE: (a–b) two frames from the *flower garden* sequence; (c) a horizontal slice through the complete spatio-temporal volume, with the arrows indicating locations of potential key frames where flow is estimated. Note that the colors for the flower garden sequence are incorrect; the correct colors (yellow flowers) are shown in Figure 9.13.

as a horizontal slice through the spatio-temporal volume, i.e., the 3D volume created by stacking all of the video frames together. Because the pixel motion is mostly horizontal, the slopes of individual (textured) pixel tracks, which correspond to their horizontal velocities, can clearly be seen. Spatio-temporal filtering uses a 3D volume around each pixel to determine the best orientation in space–time, which corresponds directly to a pixel's velocity.

Unfortunately, to obtain reasonably accurate velocity estimates everywhere in an image, spatio-temporal filters have moderately large extents, which severely degrades the quality of their estimates near motion discontinuities. (This same problem is endemic in 2D window-based motion estimators.) An alternative to full spatio-temporal filtering is to estimate more local spatio-temporal derivatives and use them inside a global optimization framework to fill in textureless regions (Bruhn, Weickert, and Schnörr 2005; Govindu 2006).

Another alternative is to simultaneously estimate multiple motion estimates, while also optionally reasoning about occlusion relationships (Szeliski 1999a). Figure 9.11c shows schematically one potential approach to this problem. The horizontal arrows show the locations of keyframes s where motion is estimated, while other slices indicate video frames t whose colors are matched with those predicted by interpolating between the keyframes. Motion estimation can be cast as a global energy minimization problem that simultaneously minimizes brightness compatibility and flow compatibility terms between keyframes and other frames, in addition to using robust smoothness terms.

The multi-view framework is potentially even more appropriate for rigid scene motion (multi-view stereo) (Section 12.7), where the unknowns at each pixel are disparities and occlusion relationships can be determined directly from pixel depths (Szeliski 1999a; Kolmogorov and Zabih 2002). However, it is also applicable to general motion, with the addition of models for occlusion relationships, as in the MirrorFlow system of Hur and Roth (2017) as well as multi-frame versions (Janai, Guney *et al.* 2018; Neoral, Šochman, and Matas 2018; Ren, Gallo *et al.* 2019).

9.3.4 *Application*: Video denoising

Video denoising is the process of removing noise and other artifacts such as scratches from film and video (Kokaram 2004; Gai and Kang 2009; Liu and Freeman 2010). Unlike single image denoising, where the only information available is in the current picture, video denoisers can average or borrow information from adjacent frames. However, to do this without introducing blur or jitter (irregular motion), they need accurate per-pixel motion estimates. One way to do this is to use task-oriented flow, where the flow network is specifically tuned end-to-end to provide the best denoising performance (Xue, Chen *et al.* 2019).

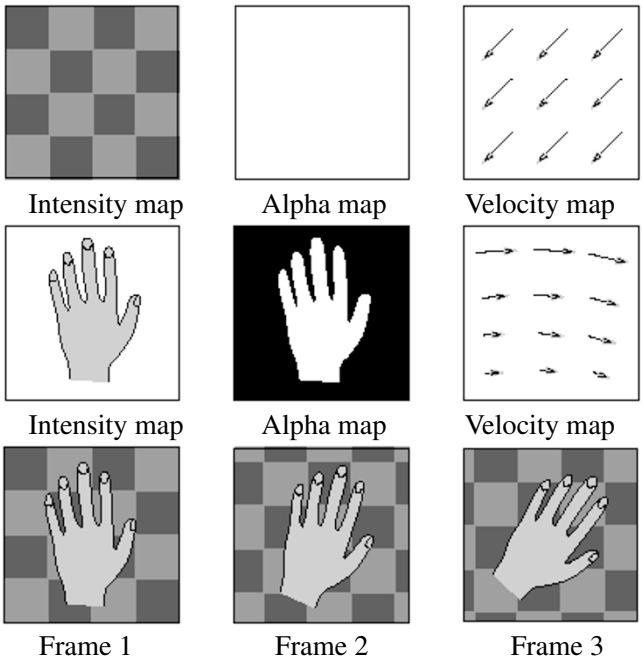

Figure 9.12 Layered motion estimation framework (Wang and Adelson 1994) © 1994 IEEE: The top two rows describe the two layers, each of which consists of an intensity (color) image, an alpha mask (black=transparent), and a parametric motion field. The layers are composited with different amounts of motion to recreate the video sequence.

Exercise 9.6 lists some of the steps required, which include the ability to determine if the current motion estimate is accurate enough to permit averaging with other frames. And while some recent papers continue to estimate flow as part of the multi-frame denoising pipeline (Tassano, Delon, and Veit 2019; Xue, Chen *et al.* 2019), others either concatenate similar patches from different frames (Maggioni, Boracchi *et al.* 2012) or concatenate small subsets of frames into a deep network that never explicitly estimates a motion representation (Claus and van Gemert 2019; Tassano, Delon, and Veit 2020). A more general form of video enhancement and restoration called *video quality mapping* has also recently started being investigated (Fuoli, Huang *et al.* 2020).

9.4 Layered motion

In many situations, visual motion is caused by the movement of a small number of objects at different depths in the scene. In such situations, the pixel motions can be described more succinctly (and estimated more reliably) if pixels are grouped into appropriate objects or *layers* (Wang and Adelson 1994).

Figure 9.12 shows this approach schematically. The motion in this sequence is caused by the translational motion of the checkered background and the rotation of the foreground hand. The complete motion sequence can be reconstructed from the appearance of the foreground and background elements, which can be represented as alpha-matted images (*sprites* or *video objects*) and the parametric motion corresponding to each layer. Displacing and compositing these layers in back to front order (Section 3.1.3) recreates the original video sequence.

Layered motion representations not only lead to compact representations (Wang and Adelson

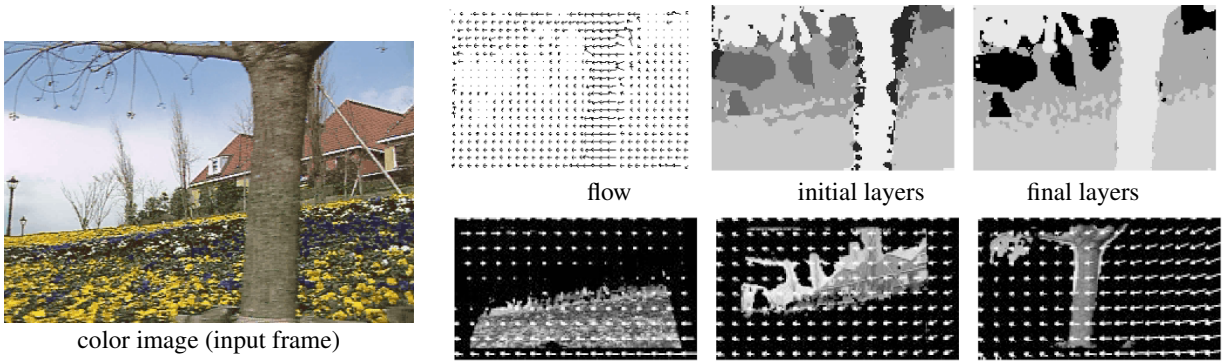

Figure 9.13 Layered motion estimation results (Wang and Adelson 1994) © 1994 IEEE.

1994; Lee, Chen *et al.* 1997), but they also exploit the information available in multiple video frames, as well as accurately modeling the appearance of pixels near motion discontinuities. This makes them particularly suited as a representation for image-based rendering (Section 14.2.1) (Shade, Gortler *et al.* 1998; Zitnick, Kang *et al.* 2004) as well as object-level video editing.

To compute a layered representation of a video sequence, Wang and Adelson (1994) first estimate affine motion models over a collection of non-overlapping patches and then cluster these estimates using k-means. They then alternate between assigning pixels to layers and recomputing motion estimates for each layer using the assigned pixels, using a technique first proposed by Darrell and Pentland (1991). Once the parametric motions and pixel-wise layer assignments have been computed for each frame independently, layers are constructed by warping and merging the various layer pieces from all of the frames together. Median filtering is used to produce sharp composite layers that are robust to small intensity variations, as well as to infer occlusion relationships between the layers. Figure 9.13 shows the results of this process on the *flower garden* sequence. You can see both the initial and final layer assignments for one of the frames, as well as the composite flow and the alpha-matted layers with their corresponding flow vectors overlaid.

In follow-on work, Weiss and Adelson (1996) use a formal probabilistic mixture model to infer both the optimal number of layers and the per-pixel layer assignments. Weiss (1997) further generalizes this approach by replacing the per-layer affine motion models with smooth regularized per-pixel motion estimates, which allows the system to better handle curved and undulating layers, such as those seen in most real-world sequences.

The above approaches, however, still make a distinction between estimating the motions and layer assignments and then later estimating the layer colors. In the system described by Baker, Szeliski, and Anandan (1998), the generative model is generalized to account for real-world rigid motion scenes. The motion of each frame is described using a 3D camera model and the motion of each layer is described using a 3D plane equation plus per-pixel residual depth offsets (the *plane plus parallax* representation (Section 2.1.4)). The initial layer estimation proceeds in a manner similar to that of Wang and Adelson (1994), except that rigid planar motions (homographies) are used instead of affine motion models. The final model refinement, however, jointly re-optimizes the layer pixel color and opacity values L_l and the 3D depth, plane, and motion parameters z_l, $\mathbf{n}_l$, and $\mathbf{P}_t$ by minimizing the discrepancy between the re-synthesized and observed motion sequences (Baker, Szeliski, and Anandan 1998).

Figure 9.14 shows the final results obtained with this algorithm. As you can see, the motion

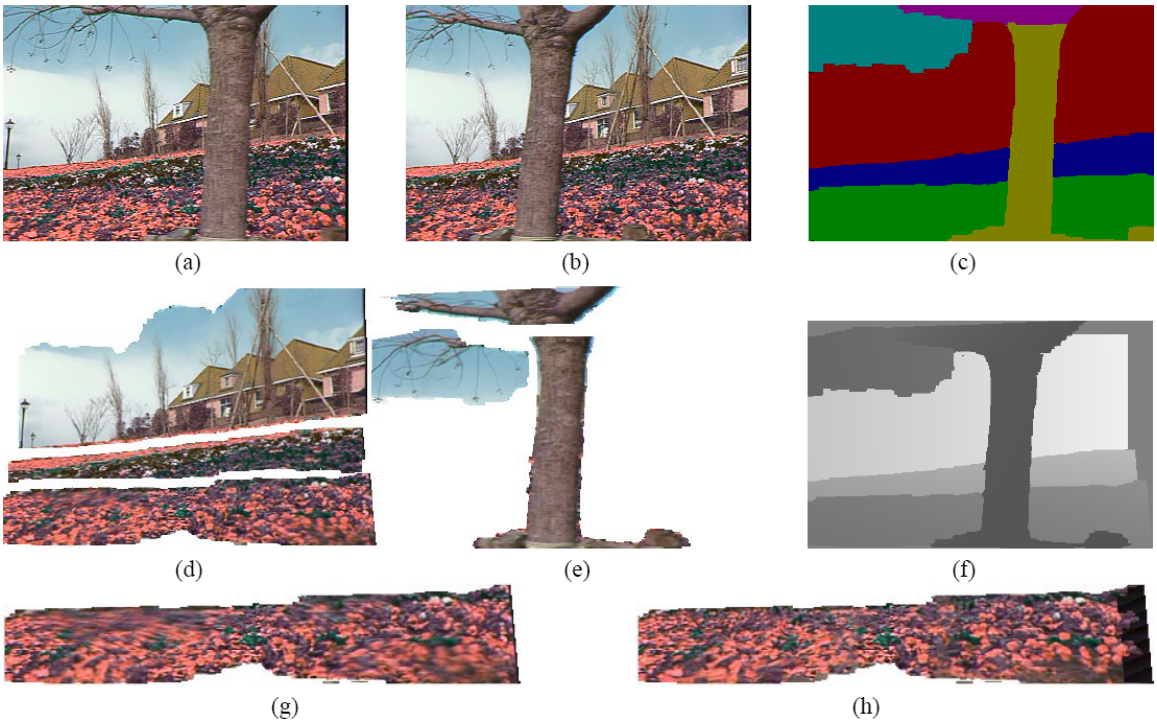

Figure 9.14 Layered stereo reconstruction (Baker, Szeliski, and Anandan 1998) © 1998 IEEE: (a) first and (b) last input images; (c) initial segmentation into six layers; (d) and (e) the six layer sprites; (f) depth map for planar sprites (darker denotes closer); front layer (g) before and (h) after residual depth estimation. Note that the colors for the flower garden sequence are incorrect; the correct colors (yellow flowers) are shown in Figure 9.13.

boundaries and layer assignments are much crisper than those in Figure 9.13. Because of the per-pixel depth offsets, the individual layer color values are also sharper than those obtained with affine or planar motion models. While the original system of Baker, Szeliski, and Anandan (1998) required a rough initial assignment of pixels to layers, Torr, Szeliski, and Anandan (2001) describe automated Bayesian techniques for initializing this system and determining the optimal number of layers.

Layered motion estimation continues to be an active area of research. Representative papers from the 2000s include (Sawhney and Ayer 1996; Jojic and Frey 2001; Xiao and Shah 2005; Kumar, Torr, and Zisserman 2008; Thayananthan, Iwasaki, and Cipolla 2008; Schoenemann and Cremers 2008), while more recent papers include (Sun, Sudderth, and Black 2012; Sun, Wulff *et al.* 2013; Sun, Liu, and Pfister 2014; Wulff and Black 2015) and (Sevilla-Lara, Sun *et al.* 2016), which jointly performs semantic segmentation and motion estimation.

Layers are not the only way to introduce segmentation into motion estimation. A large number of algorithms have been developed that alternate between estimating optical flow vectors and segmenting them into coherent regions (Black and Jepson 1996; Ju, Black, and Jepson 1996; Chang, Tekalp, and Sezan 1997; Mémin and Pérez 2002; Cremers and Soatto 2005). Some of these techniques rely on first segmenting the input color images and then estimating per-segment motions that produce a coherent motion field while also modeling occlusions (Zitnick, Kang *et al.* 2004; Zitnick, Jojic, and Kang 2005; Stein, Hoiem, and Hebert 2007; Thayananthan, Iwasaki, and Cipolla 2008). In fact, the segmentation of videos into coherently moving parts has evolved into its own topic, namely *video object segmentation*, which we study in Section 9.4.3.

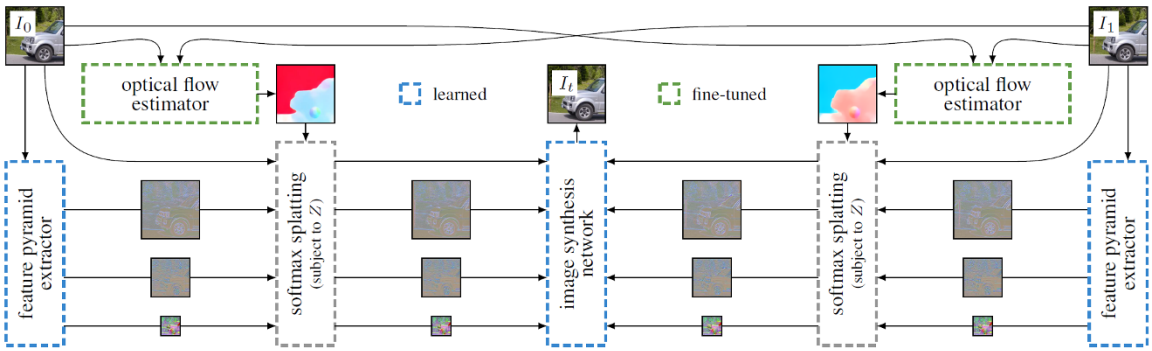

Figure 9.15 Deep feature video interpolation network (Niklaus and Liu 2020) © 2020 IEEE. This multi-stage network first computes bi-directional flow, encodes each frame using feature pyramids, and then warps and combines these features using softmax splatting. The combined features are then fed into a final image synthesis network (decoder).

9.4.1 *Application*: Frame interpolation

Frame interpolation is a widely used application of motion estimation, often implemented in hardware to match an incoming video to a monitor's actual refresh rate, where information in novel in-between frames needs to be interpolated from preceding and subsequent frames. The best results can be obtained if an accurate motion estimate can be computed at each unknown pixel's location. However, in addition to computing the motion, occlusion information is critical to prevent colors from being contaminated by moving foreground objects that might obscure a particular pixel in a preceding or subsequent frame.

In a little more detail, consider Figure 9.11c and assume that the arrows denote keyframes between which we wish to interpolate additional images. The orientations of the streaks in this figure encode the velocities of individual pixels. If the same motion estimate $\mathbf{u}_0$ is obtained at location $\mathbf{x}_0$ in image I_0 as is obtained at location $\mathbf{x}_0 + \mathbf{u}_0$ in image I_1, the flow vectors are said to be *consistent*. This motion estimate can be transferred to location $\mathbf{x}_0 + t\mathbf{u}_0$ in the image I_t being generated, where $t \in (0, 1)$ is the time of interpolation. The final color value at pixel $\mathbf{x}_0 + t\mathbf{u}_0$ can be computed as a linear blend,

$$I_t(\mathbf{x}_0 + t\mathbf{u}_0) = (1 - t)I_0(\mathbf{x}_0) + tI_1(\mathbf{x}_0 + \mathbf{u}_0). \tag{9.59}$$

If, however, the motion vectors are different at corresponding locations, some method must be used to determine which is correct and which image contains colors that are occluded. The actual reasoning is even more subtle than this. One example of such an interpolation algorithm, based on earlier work in depth map interpolation by Shade, Gortler *et al.* (1998) and Zitnick, Kang *et al.* (2004), is the one used in the flow evaluation paper of Baker, Scharstein *et al.* (2011). An even higher-quality frame interpolation algorithm, which uses gradient-based reconstruction, is presented by Mahajan, Huang *et al.* (2009). Accuracy on frame interpolation tasks is also sometimes used to gauge the quality of motion estimation algorithms (Szeliski 1999b; Baker, Scharstein *et al.* 2011).

More recent frame interpolation techniques use deep neural networks as part of their architectures. Some approaches use spatio-temporal convolutions (Niklaus, Mai, and Liu 2017), while others use DNNs to compute bi-directional optical flow (Xue, Chen *et al.* 2019) and then combine the contributions from the two original frames using either context features (Niklaus and Liu 2018) or soft visibility maps (Jiang, Sun *et al.* 2018). The system by Niklaus and Liu (2020) encodes the input frames as deep multi-resolution neural features, forward warps these using bi-directional

Figure 9.16 Light reflecting off the transparent glass of a picture frame: (a) first image from the input sequence; (b) dominant motion layer *min-composite*; (c) secondary motion residual layer *max-composite*; (d–e) final estimated picture and reflection layers The original images are from Black and Anandan (1996), while the separated layers are from Szeliski, Avidan, and Anandan (2000) © 2000 IEEE.

flow, combines these features using softmax splatting, and then uses a final deep network to decode these combined features, as shown in Figure 9.15. A similar architecture can also be used to create temporally textured looping videos from a single still image (Holynski, Curless *et al.* 2021). Other recently developed frame interpolation networks include Choi, Choi *et al.* (2020), Lee, Kim *et al.* (2020), Kang, Jo *et al.* (2020), and Park, Ko *et al.* (2020).

9.4.2 Transparent layers and reflections

A special case of layered motion that occurs quite often is transparent motion, which is usually caused by reflections seen in windows and picture frames (Figures 9.16 and 9.17).

Some of the early work in this area handles transparent motion by either just estimating the component motions (Shizawa and Mase 1991; Bergen, Burt *et al.* 1992; Darrell and Simoncelli 1993; Irani, Rousso, and Peleg 1994) or by assigning individual pixels to competing motion layers (Darrell and Pentland 1995; Black and Anandan 1996; Ju, Black, and Jepson 1996), which is appropriate for scenes partially seen through a fine occluder (e.g., foliage). However, to accurately separate truly transparent layers, a better model for motion due to reflections is required. Because of the way that light is both reflected from and transmitted through a glass surface, the correct model for reflections is an *additive* one, where each moving layer contributes some intensity to the final image (Szeliski, Avidan, and Anandan 2000).

If the motions of the individual layers are known, the recovery of the individual layers is a simple constrained least squares problem, with the individual layer images are constrained to be positive and saturated pixels provide an inequality constraint on the summed values. However, this problem can suffer from extended low-frequency ambiguities, especially if either of the layers lacks dark (black) pixels or the motion is uni-directional. In their paper, Szeliski, Avidan, and Anandan (2000) show that the simultaneous estimation of the motions and layer values can be obtained by alternating between robustly computing the motion layers and then making conservative (upper- or

Figure 9.17 Transparent motion separation (Szeliski, Avidan, and Anandan 2000) © 2000 IEEE: (a) first image from input sequence; (b) dominant motion layer *min-composite*; (c) secondary motion residual layer *max-composite*; (d–e) final estimated picture and reflection layers. Note that the reflected layers in (c) and (e) are doubled in intensity to better show their structure.

lower-bound) estimates of the layer intensities. The final motion and layer estimates can then be polished using gradient descent on a joint constrained least squares formulation similar to Baker, Szeliski, and Anandan (1998), where the *over* compositing operator is replaced with addition.

Figures 9.16 and 9.17 show the results of applying these techniques to two different picture frames with reflections. Notice how, in the second sequence, the amount of reflected light is quite low compared to the transmitted light (the picture of the girl) and yet the algorithm is still able to recover both layers.

Unfortunately, the simple parametric motion models used in Szeliski, Avidan, and Anandan (2000) are only valid for planar reflectors and scenes with shallow depth. The extension of these techniques to curved reflectors and scenes with significant depth has also been studied (Swaminathan, Kang *et al.* 2002; Criminisi, Kang *et al.* 2005; Jacquet, Hane *et al.* 2013), as has the extension to scenes with more complex 3D depth (Tsin, Kang, and Szeliski 2006). While motion sequences used to evaluate optical flow techniques have also started to include reflection and transparency (Baker, Scharstein *et al.* 2011; Butler, Wulff *et al.* 2012), the ground truth flow estimates they provide and use for evaluation only include the dominant motion at each pixel, e.g., ignoring mist and reflections.

In more recent work, Sinha, Kopf *et al.* (2012) model 3D scenes with reflections captured from a moving camera using two layers with varying depth and reflectivity and then use these to produce image-based renderings (novel view synthesis), which we discuss in more detail in Section 14.2.1. Kopf, Langguth *et al.* (2013) extend the modeling and rendering component of this system to recover colored image *gradients* for each layer and then use gradient-domain rendering to reconstruct the novel views. Xue, Rubinstein *et al.* (2015) extend these models with a gradient sparsity prior to enable *obstruction-free photography* when looking through windows and fences. More recent papers on this topic include Yang, Li *et al.* (2016), Nandoriya, Elgharib *et al.* (2017), and Liu, Lai *et al.* (2020a). The advent of dual-pixel imaging sensors, originally designed to provide fast focusing, can also be used to remove reflections by separating gradients into different depth planes (Punnappurath and Brown 2019).

While all of these techniques are useful for separating or eliminating reflections that appear as coherent images, more complex 3D geometries often give rise to spatially distributed *specularities* (Section 2.2.2) that are not amenable to layer-based representation. In such cases, lightfield representations such as surface lightfields (Section 14.3.2 and Figure 14.13) and neural light fields (Section 14.6 and Figure 14.24b) may be more appropriate.

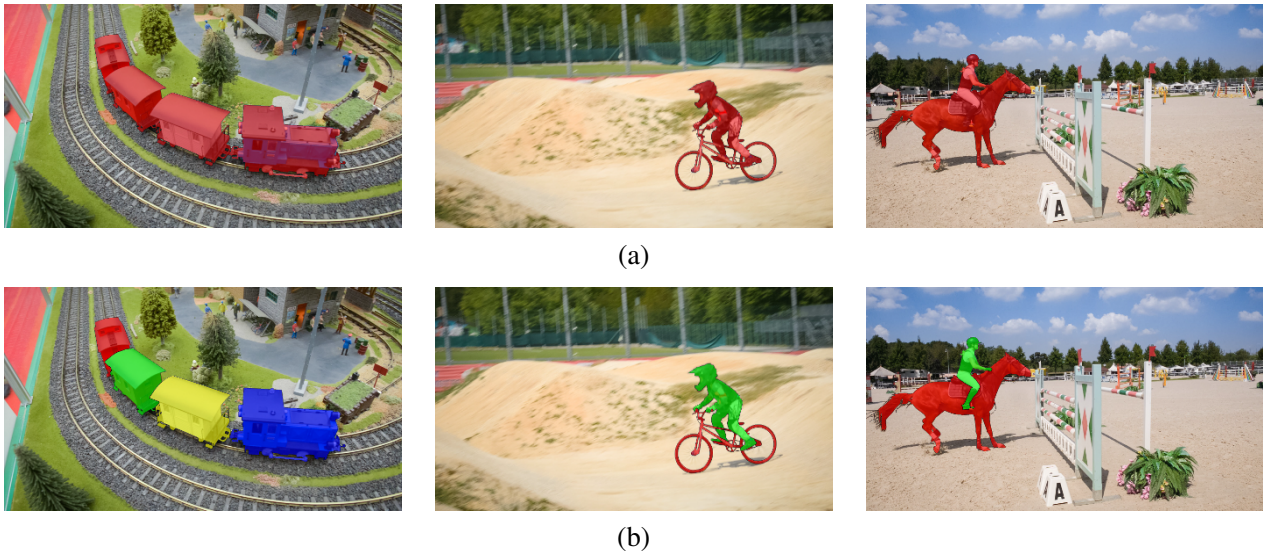

Figure 9.18 Sample sequences from the Densely Annotated VIdeo Segmentation (DAVIS) datasets © Pont-Tuset, Perazzi *et al.* (2017). The DAVIS 2016 dataset (a) only contains foreground-background segmentations (red regions), while the DAVIS 2017 dataset (b) contains multiple annotated objects in each sequence (brightly colored regions).

9.4.3 Video object segmentation

As we have seen throughout this chapter, the accurate estimation of motion usually requires the segmentation of a video into coherently moving regions or objects as well as the correct modeling of occlusions. Segmenting a video clip into coherent objects is the temporal analog to still image segmentation, which we studied in Section 7.5. In addition to providing more accurate motion estimates, video object segmentation supports a variety of editing tasks, such as object removal and insertion (Section 10.4.5) as well as video understanding and interpretation.

While the segmentation of foreground and background layers has been studied for a long time (Bergen, Anandan *et al.* 1992; Wang and Adelson 1994; Gorelick, Blank *et al.* 2007; Lee and Grauman 2010; Brox and Malik 2010b; Lee, Kim, and Grauman 2011; Fragkiadaki, Zhang, and Shi 2012; Papazoglou and Ferrari 2013; Wang, Shen, and Porikli 2015; Perazzi, Wang *et al.* 2015), the introduction of DAVIS (Densely Annotated VIdeo Segmentation) by Perazzi, Pont-Tuset *et al.* (2016) greatly accelerated research in this area. Figure 9.18a shows some frames from the original DAVIS 2016 dataset, where the first frame is annotated with a foreground pixel mask (shown in red) and the task is to estimate foreground masks for the remaining frames. The DAVIS 2017 dataset (Pont-Tuset, Perazzi *et al.* 2017) increased the number of video clips from 50 to 150, added more challenging elements such as motion blur and foreground occlusions, and most importantly, added more than one annotated object per sequence (Figure 9.18b).

Algorithm for video object segmentation such as OSVOS (Caelles, Maninis *et al.* 2017), FusionSeg (Jain, Xiong, and Grauman 2017), MaskTrack (Perazzi, Khoreva *et al.* 2017), and SegFlow (Cheng, Tsai *et al.* 2017), usually consist of a deep per-frame segmentation network as well as a motion estimation algorithm, which is used to link and refine the segmentations. Some approaches (Caelles, Maninis *et al.* 2017; Khoreva, Benenson *et al.* 2019) also fine-tune the segmentation networks based on the first frame annotations. More recent approaches have focused on increasing the computational efficiency of the pipelines (Chen, Pont-Tuset *et al.* 2018; Cheng, Tsai *et al.* 2018;

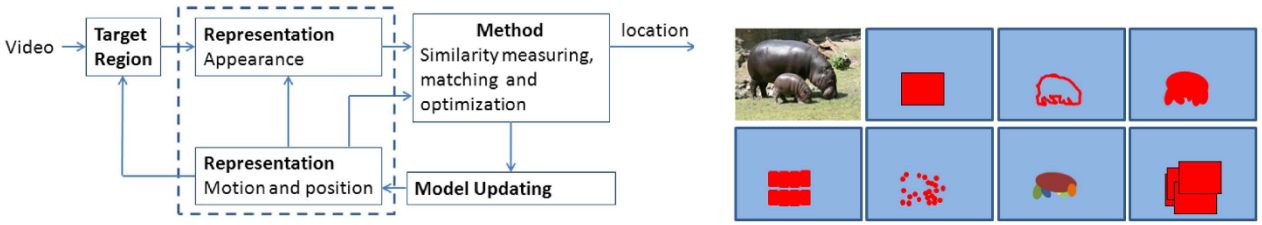

Figure 9.19 Visual object tracking (Smeulders, Chu *et al.* 2014) ©2014 IEEE: (a) high-level model showing main tracker components; (b) some tracked region representations, including a single bounding box, contour, blob, patch-based, sparse features, parts, and multiple bounding boxes.

Wug Oh, Lee *et al.* 2018; Wang, Zhang *et al.* 2019; Meinhardt and Leal-Taixé 2020).

Since 2017, an annual challenge and workshop on the DAVIS dataset have been held in conjunction with CVPR. More recent additions to the challenges have been segmentation with weaker annotations/scribbles (Caelles, Montes *et al.* 2018) or completely unsupervised segmentation, where the algorithms compute temporally linked segmentations of the video frames (Caelles, Pont-Tuset *et al.* 2019). There is also a newer, larger, dataset called YouTube-VOS (Xu, Yang *et al.* 2018) with its own associated set of challenges and leaderboards. The number of papers published on the topic continues to be high. The best sources for recent work are the challenge leaderboards at https://davischallenge.org and https://youtube-vos.org, which are accompanied by short papers describing the techniques, as well as the large number of conference papers, which usually have "Video Object Segmentation" in their titles.

9.4.4 Video object tracking

One of the most widely used applications of computer vision to video analysis is *video object tracking*. These applications include surveillance (Benfold and Reid 2011), animal and cell tracking (Khan, Balch, and Dellaert 2005), sports player tracking (Lu, Ting *et al.* 2013), and automotive safety (Janai, Güney *et al.* 2020, Chapter 6).

We have already discussed simpler examples of tracking in previous chapters, including feature (patch) tracking in Section 7.1.5 and contour tracking in Section 7.3. Surveys and experimental evaluation of such techniques include Lepetit and Fua (2005), Yilmaz, Javed, and Shah (2006), Wu, Lim, and Yang (2013), and Janai, Güney *et al.* (2020, Chapter 6).

A great starting point for learning more about tracking is the survey and tutorial by Smeulders, Chu *et al.* (2014), which was also one of the first large-scale tracking datasets, with over 300 video clips, ranging from a few seconds to a few minutes. Figure 9.19a shows some of the main components usually present in an online tracking system, which include choosing representations for shape, motion, position, and appearance, as well as similarity measures, optimization, and optional model updating. Figure 9.19b shows some of the choices for representing shapes and appearance, including a single bounding box, contours, patches, features, and parts.

The paper includes a discussion of previous surveys and techniques, as well as datasets, evaluation measures, and the above-mentioned model choices. It then categorizes a selection of well-known and more recent algorithms into a taxonomy that includes simple matching with fixed templates, extended and constrained (sparse) appearance models, discriminative classifiers, and tracking by detection. The algorithms discussed and evaluated include KLT, as implemented by Baker and Matthews (2004), mean-shift (Comaniciu and Meer 2002) and fragments-based (Adam, Rivlin, and

Shimshoni 2006) tracking, online PCA appearance models (Ross, Lim *et al.* 2008), sparse bases (Mei and Ling 2009), and Struct (Hare, Golodetz *et al.* 2015), which uses kernelized structured output support vector machine.

Around the same time (2013), a series of annual challenges and workshops on single-target short-term tracking called VOT (visual object tracking) began.[21] In their journal paper describing the evaluation methodology, Kristan, Matas *et al.* (2016) evaluate recent trackers and find that variants of Struct as well as extensions of kernelized correlation filters (KCF), originally developed by Henriques, Caseiro *et al.* (2014), performed the best. Other highly influential papers from this era include (Bertinetto, Valmadre *et al.* 2016a,b; Danelljan, Robinson *et al.* 2016). Since that time, deep networks have played an essential role in visual object tracking, often using Siamese networks (Section 5.3.4; Bromley, Guyon *et al.* 1994; Chopra, Hadsell, and LeCun 2005) to map regions being tracked into neural embeddings. Lists and descriptions of more recent tracking algorithms can be found in the annual reports that accompany the VOT challenges and workshops, the most recent of which is Kristan, Leonardis *et al.* (2020).

In parallel with the single-object VOT challenges and workshops, a multiple object tracking was introduced as part of the KITTI vision benchmark (Geiger, Lenz, and Urtasun 2012) and a separate benchmark was developed by Leal-Taixé, Milan *et al.* (2015) along with a series of challenges, with the most recent results described in Dendorfer, Ošep *et al.* (2021).[22] A survey of multiple object tracking papers through 2016 can be found in Luo, Xing *et al.* (2021). Simple and fast multiple object trackers include Bergmann, Meinhardt, and Leal-Taixé (2019) and Zhou, Koltun, and Krähenbühl (2020). Until recently, however, tracking datasets have focused mostly on people, vehicles, and animals. To expand the range of objects that can be tracked, Dave, Khurana *et al.* (2020) created the TAO (tracking any object) dataset, consisting of 2,907 videos, which were annotated "bottom-up" by first having users tag anything that moves and then classifying such objects into 833 categories.

While in this section, we have focused mostly on object tracking, the primary goal of which is to locate an object in contiguous video frames, it is also possible to simultaneously track and segment (Voigtlaender, Krause *et al.* 2019; Wang, Zhang *et al.* 2019) or to track non-rigidly deforming objects such as T-shirts with deformable models from either video (Kambhamettu, Goldgof *et al.* 2003; White, Crane, and Forsyth 2007; Pilet, Lepetit, and Fua 2008; Furukawa and Ponce 2008; Salzmann and Fua 2010) or RGB-D streams (Božič, Zollhöfer *et al.* 2020; Božič, Palafox *et al.* 2020, 2021). The recent TrackFormer paper by Meinhardt, Kirillov *et al.* (2021) includes a nice review of recent work of multi-object tracking and segmentation.

9.5 Additional reading

Some of the earliest algorithms for motion estimation were developed for motion-compensated video coding (Netravali and Robbins 1979) and such techniques continue to be used in modern coding standards such as MPEG, H.263, and H.264 (Le Gall 1991; Richardson 2003).[23] In computer vision, this field was originally called *image sequence analysis* (Huang 1981). Some of the early seminal papers include the variational approaches developed by Horn and Schunck (1981) and Nagel and Enkelmann (1986), and the patch-based translational alignment technique developed by Lucas and Kanade (1981). Hierarchical (coarse-to-fine) versions of such algorithms were developed by Quam

[21] https://www.votchallenge.net
[22] https://motchallenge.net
[23] https://www.itu.int/rec/T-REC-H.264.

(1984), Anandan (1989), and Bergen, Anandan *et al.* (1992), although they have also long been used in motion estimation for video coding.

Translational motion models were generalized to affine motion by Rehg and Witkin (1991), Fuh and Maragos (1991), and Bergen, Anandan *et al.* (1992) and to quadric reference surfaces by Shashua and Toelg (1997) and Shashua and Wexler (2001)—see Baker and Matthews (2004) for a nice review. Such parametric motion estimation algorithms have found widespread application in video summarization (Teodosio and Bender 1993; Irani and Anandan 1998), video stabilization (Hansen, Anandan *et al.* 1994; Srinivasan, Chellappa *et al.* 2005; Matsushita, Ofek *et al.* 2006), and video compression (Irani, Hsu, and Anandan 1995; Lee, Chen *et al.* 1997). Surveys of parametric image registration include those by Brown (1992), Zitov'aa and Flusser (2003), Goshtasby (2005), and Szeliski (2006a).

Good general surveys and comparisons of optical flow algorithms include those by Aggarwal and Nandhakumar (1988), Barron, Fleet, and Beauchemin (1994), Otte and Nagel (1994), Mitiche and Bouthemy (1996), Stiller and Konrad (1999), McCane, Novins *et al.* (2001), Szeliski (2006a), and Baker, Scharstein *et al.* (2011), Sun, Yang *et al.* (2018), Janai, Güney *et al.* (2020), and Hur and Roth (2020). The topic of matching primitives, i.e., pre-transforming images using filtering or other techniques before matching, is treated in a number of papers (Anandan 1989; Bergen, Anandan *et al.* 1992; Scharstein 1994; Zabih and Woodfill 1994; Cox, Roy, and Hingorani 1995; Viola and Wells III 1997; Negahdaripour 1998; Kim, Kolmogorov, and Zabih 2003; Jia and Tang 2003; Papenberg, Bruhn *et al.* 2006; Seitz and Baker 2009). Hirschmüller and Scharstein (2009) compare a number of these approaches and report on their relative performance in scenes with exposure differences.

The publication of the first large benchmark for evaluating optical flow algorithms by Baker, Scharstein *et al.* (2011) led to rapid advances in the quality of estimation algorithms. While most of the best performing algorithms used robust data and smoothness norms such as L_1 or TV and continuous variational optimization techniques, some algorithms used discrete optimization or segmentation (Papenberg, Bruhn *et al.* 2006; Trobin, Pock *et al.* 2008; Xu, Chen, and Jia 2008; Lempitsky, Roth, and Rother 2008; Werlberger, Trobin *et al.* 2009; Lei and Yang 2009; Wedel, Cremers *et al.* 2009).

The creation of the Sintel (Butler, Wulff *et al.* 2012) and KITTI (Geiger, Lenz, and Urtasun 2012) datasets further accelerated progress in optical flow algorithms. Significant papers from this past decade include Weinzaepfel, Revaud *et al.* (2013), Sun, Roth, and Black (2014), Revaud, Weinzaepfel *et al.* (2015), Ilg, Mayer *et al.* (2017), Xu, Ranftl, and Koltun (2017), Sun, Yang *et al.* (2018, 2019), Hur and Roth (2019), and Teed and Deng (2020b). Good review of flow papers from the last decade can be found in Sun, Yang *et al.* (2018), Janai, Güney *et al.* (2020), and Hur and Roth (2020).

Good starting places to read about video object segmentation and video object tracking are recent workshops associated with the main datasets and challenges on these topics (Pont-Tuset, Perazzi *et al.* 2017; Xu, Yang *et al.* 2018; Kristan, Leonardis *et al.* 2020; Dave, Khurana *et al.* 2020; Dendorfer, Ošep *et al.* 2021).

9.6 Exercises

Ex 9.1: Correlation. Implement and compare the performance of the following correlation algorithms:

- sum of squared differences (9.1)
- sum of robust differences (9.2)

- sum of absolute differences (9.3)
- bias–gain compensated squared differences (9.9)
- normalized cross-correlation (9.11)
- windowed versions of the above (9.22–9.23)
- Fourier-based implementations of the above measures (9.18–9.20)
- phase correlation (9.24)
- gradient cross-correlation (Argyriou and Vlachos 2003).

Compare a few of your algorithms on different motion sequences with different amounts of noise, exposure variation, occlusion, and frequency variations (e.g., high-frequency textures, such as sand or cloth, and low-frequency images, such as clouds or motion-blurred video). Some datasets with illumination variation and ground truth correspondences (horizontal motion) can be found at https://vision.middlebury.edu/stereo/data (the 2005 and 2006 datasets).

Some additional ideas, variants, and questions:

1. When do you think that phase correlation will outperform regular correlation or SSD? Can you show this experimentally or justify it analytically?
2. For the Fourier-based masked or windowed correlation and sum of squared differences, the results should be the same as the direct implementations. Note that you will have to expand (9.5) into a sum of pairwise correlations, just as in (9.22). (This is part of the exercise.)
3. For the bias–gain corrected variant of squared differences (9.9), you will also have to expand the terms to end up with a 3×3 (least squares) system of equations. If implementing the Fast Fourier Transform version, you will need to figure out how all of these entries can be evaluated in the Fourier domain.
4. (Optional) Implement some of the additional techniques studied by Hirschmüller and Scharstein (2009) and see if your results agree with theirs.

Ex 9.2: Affine registration. Implement a coarse-to-fine direct method for affine and projective image alignment.

1. Does it help to use lower-order (simpler) models at coarser levels of the pyramid (Bergen, Anandan *et al.* 1992)?
2. (Optional) Implement patch-based acceleration (Shum and Szeliski 2000; Baker and Matthews 2004).
3. See the Baker and Matthews (2004) survey for more comparisons and ideas.

Ex 9.3: Stabilization. Write a program to stabilize an input video sequence. You could implement the following steps, as described in Section 9.2.1:

1. Compute the translation (and, optionally, rotation) between successive frames with robust outlier rejection.
2. Perform temporal high-pass filtering on the motion parameters to remove the low-frequency component (smooth the motion).

3. Compensate for the high-frequency motion, zooming in slightly (a user-specified amount) to avoid missing edge pixels.
4. (Optional) Do not zoom in, but instead borrow pixels from previous or subsequent frames to fill in.
5. (Optional) Compensate for images that are blurry because of fast motion by "stealing" higher frequencies from adjacent frames.

Ex 9.4: Optical flow. Compute optical flow (spline-based or per-pixel) between two images, using one or more of the techniques described in this chapter.

1. Test your algorithms on the motion sequences available at https://vision.middlebury.edu/flow or http://sintel.is.tue.mpg.de and compare your results (visually) to those available on these websites. If you think your algorithm is competitive with the best, consider submitting it for formal evaluation.
2. Visualize the quality of your results by generating in-between images using frame interpolation (Exercise 9.5).
3. What can you say about the relative efficiency (speed) of your approach?

Ex 9.5: Automated morphing and frame interpolation. Write a program to automatically morph between pairs of images. Implement the following steps, as sketched out in Section 9.4.1 and by Baker, Scharstein *et al.* (2011):

1. Compute the flow both ways (previous exercise). Consider using a multi-frame ($n > 2$) technique to better deal with occluded regions.
2. For each intermediate (morphed) image, compute a set of flow vectors and which images should be used in the final composition.
3. Blend (cross-dissolve) the images and view with a sequence viewer.

Try this out on images of your friends and colleagues and see what kinds of morphs you get. Alternatively, take a video sequence and do a high-quality slow-motion effect. Compare your algorithm with simple cross-fading.

Ex 9.6: Video denoising. Implement the algorithm sketched in Application 9.3.4. Your algorithm should contain the following steps:

1. Compute accurate per-pixel flow.
2. Determine which pixels in the reference image have good matches with other frames.
3. Either average all of the matched pixels or choose the sharpest image, if trying to compensate for blur. Don't forget to use regular single-frame denoising techniques as part of your solution, (see Section 3.4.2 and Exercise 3.12).
4. Devise a fall-back strategy for areas where you don't think the flow estimates are accurate enough.

Ex 9.7: Layered motion estimation. Decompose into separate layers (Section 9.4) a video sequence of a scene taken with a moving camera:

1. Find the set of dominant (affine or planar perspective) motions, either by computing them in blocks or by finding a robust estimate and then iteratively re-fitting outliers.
2. Determine which pixels go with each motion.
3. Construct the layers by blending pixels from different frames.
4. (Optional) Add per-pixel residual flows or depths.
5. (Optional) Refine your estimates using an iterative global optimization technique.
6. (Optional) Write an interactive renderer to generate in-between frames or view the scene from different viewpoints (Shade, Gortler *et al.* 1998).
7. (Optional) Construct an *unwrap mosaic* from a more complex scene and use this to do some video editing (Rav-Acha, Kohli *et al.* 2008).

Ex 9.8: Transparent motion and reflection estimation. Take a video sequence looking through a window (or picture frame) and see if you can remove the reflection to better see what is inside.

The steps are described in Section 9.4.2 and by Szeliski, Avidan, and Anandan (2000). Alternative approaches can be found in work by Shizawa and Mase (1991), Bergen, Burt *et al.* (1992), Darrell and Simoncelli (1993), Darrell and Pentland (1995), Irani, Rousso, and Peleg (1994), Black and Anandan (1996), and Ju, Black, and Jepson (1996).

Ex 9.9: Motion segmentation. Write a program to segment an image into separately moving regions or to reliably find motion boundaries.

Use the DAVIS motion segmentation database (Pont-Tuset, Perazzi *et al.* 2017) as some of your test data.

Ex 9.10: Video object tracking. Write an object tracker and test it out on one of the latest video object tracking datasets (Leal-Taixé, Milan *et al.* 2015; Kristan, Matas *et al.* 2016; Dave, Khurana *et al.* 2020; Kristan, Leonardis *et al.* 2020; Dendorfer, Ošep *et al.* 2021).